Geophys. J. Int. (1994) **119**, 428–452

ISSN 0956-540X

Seamount topography by least-squares inversion of altimetric geoid heights and shipborne profiles of bathymetry and/or gravity anomalies

Stéphane Calmant

Equipe de Géologie-Géophysique, Centre ORSTOM de Nouméa, BP A5, *Nouméa, New Caledonia, South West Pacific*

Accepted 1994 March 22. Received 1994 March 18; in original form 1993 March 25

SUMMARY

Altimetric measurements of sea-surface heights have long been used to locate uncharted marine features. Newly available data sets (Geosat-GM, ERS-1 and Topex/Poséïdon), now allow the topography of submarine volcanoes to be accurately restored and a method based upon inverse modelling is presented in this paper. This method allows a joint assimilation of altimetric data and shipborne profiles of bathymetry and/or gravity anomalies when available. Furthermore, uncertainties can be computed together with the topography, which constitutes a noticeable improvement since these parameters are still missing in the usual bathymetric data bases. Tests are performed using simulated data, in order to characterize the errors which may or must occur with the modelled topography of a previously unknown volcano, in particular the errors due to data uncertainties and the lack of precise knowledge of sensitive parameters that are used in the modelling. These errors can be maintained under the 100 m level (rms) for altimetric data with a measurement noise of 5 cm (rms) or less, which is achieved for Geosat, ERS-1 and Topex/Poséïdon altimeters. An example of inversion of Seasat data is presented in the case of a seamount in French Polynesia.

Key words: altimetry, least-squares inversion, seamount topography.

1 INTRODUCTION

Bathymetry represents a basic data set for a great variety of geophysical studies in the oceans of the World. It also plays an important part in the economy, mainly in the evaluation and development of living and mineral resources as well as for marine communication cables, submarine navigation and even for ships, since uncharted shallow edifices are still encountered. However, in spite of the effort of many oceanographical institutions during the past decades, sea-floor topography is still very poorly known in many oceanic areas. Moreover, the ship-track distribution is very unequal: most of them are located in the Northern Hemisphere whereas in the Southern Hemisphere, most of the tracks run along the continental coastlines and around the main islands. As a consequence, large portions of the Indian, South Pacific and South Altantic oceans remain devoid of direct measurements. Recently, Vogt & Jung (1991) advocated an international effort to improve the current bathymetry databases. When bathymetry is performed by oceanographic vessels, it is a very expensive and time-consuming proposition. Even if the most recent techniques (Sea Mark and enlarged Seabeams) were used, it would take decades to cover the entire sea-floor. Vogt & Jung thus proposed to incorporate all the geophysical data that can be converted into bathymetric ones, such as shipborne gravity anomalies and geoid heights from satellite altimetry.

Gravity (in a large sense) has long been used for bathymetric purposes such as the detection and positioning of uncharted structures (Lambeck & Coleman 1982; Lazarewicz & Schwank 1982; Sandwell 1984; Baudry 1988) or modelling of submarine topographies (Dixon *et al.* 1983; Baudry, Diament & Albouy 1987; Baudry & Calmant 1991; Jung & Vogt 1992; Goodwillie & Watts 1993). Most of these works were conducted in the Fourier Domain to convert geoid height profiles into bathymetric profiles. This was mostly directed by the mathematical simplicity and by the way by the speed of the computations. The drawbacks are: the profiles of data need to be regularly resampled; the spectra of the these data profiles have to be lowpass filtered for the short-wavelength altimetric noise not to blow up in the bathymetric solution; the bathymetric profiles have then

to be interpolated if 3-D maps are wished; the data set cannot be made with data of a different kind; and, last, that these resulting bathymetric grids cannot be directly accompanied by any quality information. Baudry & Calmant (1991) went to step further using a pair of Seasat tracks to precisely map the topography of a submarine volcano in French Polynesia, South Pacific. They used the collocation method to get a grid of regularly spaced geoid heights from the Seasat tracks and Fourier Transforms to convert these geoid heights into bathymetry. Their results show that the restitution of such a feature can be achieved up to 90 per cent in depths and with less than 10 km of mispositioning. Besides, this was the first attempt to deal with the question of the accuracy of interpolated values, an element that is dramatically lacking in the usual bathymetric data bases such as DBDB5 or SYNBAPS (Van Wickhouse 1973). Indeed, Vogt & Jung (1991) do not address this aspect of the production of bathymetric data. In fact, the problem with errors in DBDB5 that they report must not be construed as a requirement to separate the right values from the wrong ones but as providing values with an associated uncertainty which may take on continuous and variable values over the mapped area.

In the present paper, it is intended to test the representation of the topography of seamounts using a forward modelling based on the discrete inverse theory (Menke 1984; Tarantola 1987). When using such a method, the data set may be comprised of data of different types. These are basically altimetric measurements, to which shipborne profiles of bathymetry and/or gravity anomalies may be incorporated when available. With the inverse method, uncertainties linked to the modelled values of seamount topography may also be produced. Unlike the previous works using Fourier Transforms, the spatial distribution of the data is accounted for without the need for interpolation. The error budget of the data set, which moreover may differ from one subset to another within data of the same type (for geoid heights from different satellites, for example), is also entered in the modelling.

The relationship between seamount topography and bathymetric profiles is straightforward. As far as the gravity and geoid data are concerned, there is no linear relationship between the seamount topography and the data. In this instance, the solution is reached by using iteratively improved linearized forms of the exact relationship (quasi-Newton method). Moreover, seamount topography is not the only density contrast represented in the data. The underlying upper lithosphere also presents density contrasts, the gravity signature of which is superimposed upon that of the bathymetric feature. These lithospheric density contrasts are due to the compensation of the bathymetric feature. Two models of compensation are used in the present study: the regional compensation and the local compensation. In a context of regional compensation, the shape of the density interfaces is modelled as the response to loading of a thin elastic plate. This model of shape is currently applied to intraplate volcanoes that are emplaced on an old oceanic lithosphere (assumption of elastic behaviour of the upper lithosphere related to the cooling whilst aging; McNutt & Menard 1978; Watts 1979; Cazenave *et al.* 1980; Watts & Ribe 1984; Calmant, Cazenave & Francheteau 1990) or to volcanoes which emplaced recently (assumption of visocelastic behaviour of the upper lithosphere, Lambeck & Nakiboglu 1980; Lambeck 1981a,b). The Airy model is used for the local compensation. It applies for either on ridge volcanoes in the assumption of elastic behaviour or volcanoes that emplaced long ago with respect to the characteristic time of relaxation in the assumption of visoelastic behaviour. The local compensation can also be used for modelling wide structures such as marine plateaus (Black & McAdoo 1988) or elongated ridges of presumed continental core.

To test the capability of each type of data and of combinations of various types in resolving a seamount topography, modellings are performed with synthetic data over a volcano of pre-defined topography and geophysical setting. The uncertainties associated to the modelled values are also compared to the actual errors in order to see how relevant they are.

A case study is then presented in the modelling of the topography of a seamount in French Polynesia.

2 METHOD

The topographic heights of the sea-floor are computed as the least-squares solution for model parameters of a discrete inverse problem. These model parameters consist in fact of different geophysical quantities according to the data type. For bathymetric data, the topographic heights correspond to weighted averaged heights over a reference depth upon surface elements. When gravity or geoid data are used, the modelled topographic heights correspond to the height of volumes based upon the surface elements and forming a predefined density contrast with the surrounding seawater. The solution is constructed by a linear combination of the data with optimal coefficients. These optimal coefficients are determined by the physical relationship between each datum and each model parameter, including an iteratively adjusted model, *a priori* information on the model parameters and are the description of the errors which affect the data (Tarantola 1987). $b_n(\mathbf{r})$, the modelled seamount topography at location $\mathbf{r}$ and *a posteriori* value of the model parameters for the nth iteration, is given by:

$$b_n(\mathbf{r}) = b_0(\mathbf{r}) + \mathbf{C}_{rr'}\mathbf{G}_n^T[\mathbf{G}_n\mathbf{C}_{rr'}\mathbf{G}_n^T + \mathbf{E}_{ss'}]^{-1}\{d_\tau(\mathbf{s}) - g_\tau[b_0(\mathbf{r})] + \mathbf{G}_n[b_{n-1}(\mathbf{r}) - b_0(\mathbf{r})]\} \quad (1)$$

where $b_0(\mathbf{r})$ is the vector that contains the *a priori* values of the model parameters (seamount topography at location $\mathbf{r}$) and where $b_{n-1}(\mathbf{r})$ is the vector that contains the *a posteriori* values of the model parameters for the $n-1$th iteration. $\mathbf{C}_{rr'}$ is the covariance matrix of the *a priori* model-parameter errors. $\mathbf{E}_{ss'}$ is the data-error covariance matrix. $\mathbf{G}_n$, and its transpose $\mathbf{G}_n^T$, is the matrix the elements of which are given by a linear approximation of the data functionals $g_\tau(\mathbf{s})$. τ refers to the data type, $\tau = ST$ stands for seamount topography, $\tau = GH$ for geoid heights undulations and $\tau = GA$ for gravity anomalies. $d_\tau(\mathbf{s})$ is the

Table 1. List of symbols for the geophysical parameters.

NAME	SYMBOL	VALUE (SI units)
Gravity Constant :	G	6.67 10^{-11}
Earth parameters:		
Earth radius	a	6 378 10^3
Mean gravity	γ	9.81
Lithospheric parameters:		
Seafloor depth	R_{sf}	
depth of layer 2 / 3 Interface	$R_{2/3}$	
Moho depth	R_m	
volcano (load) density	ρ_v	
density of infilling sediments	ρ_s	
density of crustal layer 2	ρ_2	
density of crustal layer 3	ρ_3	
mantle density	ρ_m	
Plate stiffness	D	
Flexural length	α	

vector that contains the data values at locations **s**. The uncertainties associated with the model values are given by (Tarantola 1987):

$$\sigma(\mathbf{r}) = \sqrt{\mathbf{C}'_{rr'}(\mathbf{r}=\mathbf{r}')} \tag{2}$$

with $\mathbf{C}'_{rr'}$, the *a posteriori* covariance matrix of the model parameters given by:

$$\mathbf{C}'_{rr'} = \mathbf{C}_{rr'} - \mathbf{C}_{rr'}\mathbf{G}_N^T[\mathbf{G}_N\mathbf{C}_{rr'}\mathbf{G}_N^T + \mathbf{E}_{ss'}]^{-1}\mathbf{G}_N\mathbf{C}_{rr'}, \tag{3}$$

where N is the last iteration, when convergence is achieved.

2.1 Data functionals and associated linear operators

The symbols standing for the geophysical parameters entering in the ongoing formulae throughout the paper are listed in Table 1. In this part, only the final form of algebraic expressions are given. Detailed developments are provided in the Appendices.

(a) Ship tracks of sea-floor topography

When the data and model parameters represent respectively sampled and interpolated values of the same geophysical function, the functional is readily given by:

$$g_{ST}(\mathbf{s}) = \int_S (\cdot)\,\delta(\mathbf{s},\mathbf{r})\,d\mathbf{r} \tag{4}$$

where $\delta()$ is the Dirac impulse and S the interpolation domain. The corresponding linear operator is:

$$\mathbf{G}(\mathbf{s},\mathbf{r},\tau=ST) = \delta(\mathbf{s},\mathbf{r}). \tag{5}$$

(b) Geoid heights and gravity anomalies

For the particular case of seamounts, lithospheric density contrasts (the shape of which is related to the height $b(\mathbf{r})$ of the structure) must be taken into account together with the density contrast between seawater and seamount. These contrasts of density are defined relative to a reference layering of the upper oceanic lithsophere. For a regionally compensated structure (flexural parameter $\alpha \neq 0$, see Appendix 2), the lithospheric density contrasts are due to the elastic deflection $w(\mathbf{r}')$ of the upper lithosphere under the weight of the volcano element of volume $\Delta\Omega(\mathbf{r})b(\mathbf{r})$ (see Fig. 1). In the case of a locally compensated structure (flexural parameter $\alpha = 0$), a light root $t(\mathbf{r})$ provides the isostatic equilibrium (see Appendix 2). The data functionals relating the model parameters $b(\mathbf{r})$ to a datum of geoid height or gravity anomaly are given by the classical expressions of the gravity anomalies or geoid heights computed for a set of density interfaces defined on grid nodes. These are reported in Appendices 3 and 4. These data functionals are not linear in $b(\mathbf{r})$ (see Appendix 3). Iterative linear approximations are thus performed to generate the linear operator $\mathbf{G}_n$ in eqs (2) and (3).

For a datum of geoid height, in the context of regional compensation and at the nth iteration, $\mathbf{G}_n$ is:

$$\mathbf{G}_n(\mathbf{s},\mathbf{r},\tau=GH,\alpha\neq 0) = \frac{\Gamma}{\gamma}\Delta\Omega(\mathbf{r})\left\{(\rho_v-\rho_w)u\left(R_{sf}+\frac{b_{n-1}(\mathbf{r})}{2},\psi_{sr}\right)+\frac{(\rho_v-\rho_w)R_{sf}^2}{\pi(\rho_m-\rho_s)\alpha^2}\sum_{\mathbf{r}'\in S}\Delta\Omega(\mathbf{r}')\,\mathrm{Kei}\left(\sqrt{2}\frac{|\mathbf{r}-\mathbf{r}'|}{\alpha}\right)\right.$$
$$\left.\times\left[(\rho_s-\rho_2)u\left(R_{sf}+\frac{w_{n-1}(\mathbf{r}')}{2},\psi_{rr'}\right)+(\rho_2-\rho_3)u\left(R_{2/3}+\frac{w_{n-1}(\mathbf{r}')}{2},\psi_{rr'}\right)+(\rho_3-\rho_m)u\left(R_m+\frac{w_{n-1}(\mathbf{r}')}{2},\psi_{rr'}\right)\right]\right\} \tag{6}$$

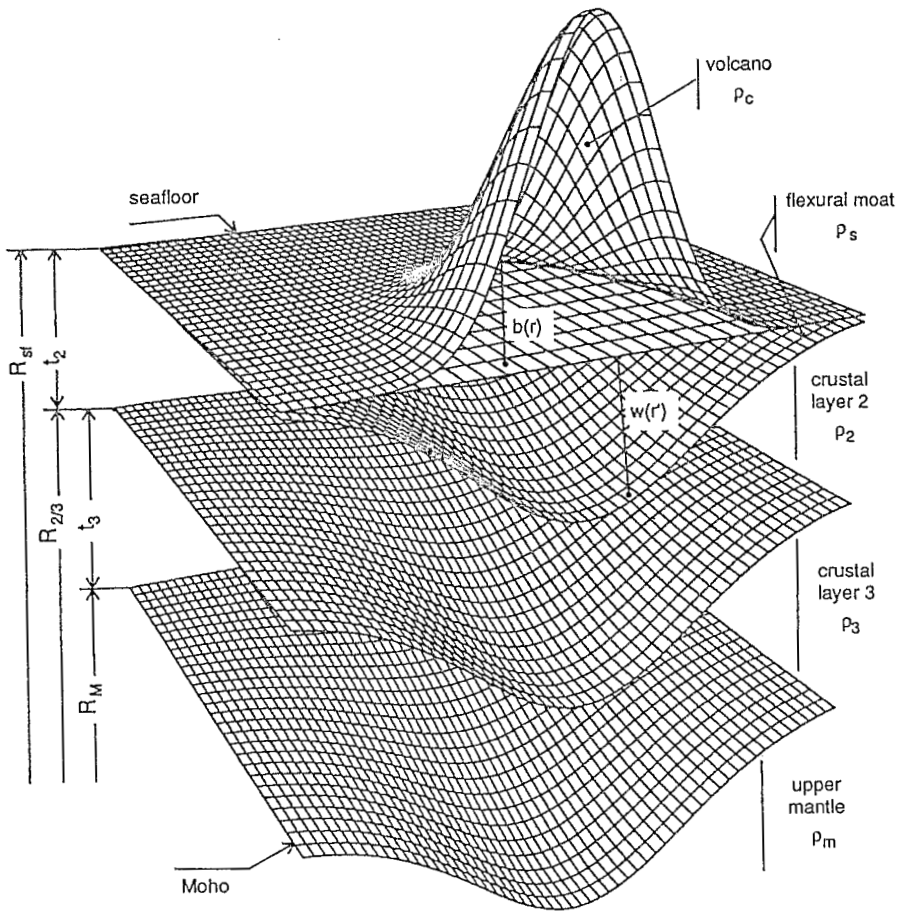

Figure 1. Geophysical setting. A volcano emplaced on the oceanic lithosphere deflects the upper layers of the lithosphere and generates lateral density contrasts with respect to the reference undeformed lithosphere. $b(r)$ and $w(r')$ respectively stand for the seamount topography and the lithospheric deflection. Other symbols are listed in Table 1.

with

$$u(R,\psi)=\frac{R^2}{\sqrt{a^2+R^2-2aR\cos\psi}}. \tag{7}$$

$\psi_{rr'}$ is the angle between locations $\mathbf{r}$ and $\mathbf{r}'$ of model parameters. Kei ( ) is the Kelvin–Bessel function.

For a datum of geoid height, in context of local compensation and at the nth iteration, $\mathbf{G}_n$ is:

$$\mathbf{G}_n(\mathbf{s},\mathbf{r},\tau=GH,\alpha=0)=\frac{\Gamma}{\gamma}\Delta\Omega(\mathbf{r})(\rho_v-\rho_w)\left[u\left(R_{sf}+\frac{b_{n-1}(\mathbf{r})}{2},\psi_{sr}\right)-u\left(R_m+\frac{t_{n-1}(\mathbf{r})}{2},\psi_{sr}\right)\right]. \tag{8}$$

For a datum of gravity anomaly, in context of regional compensation and at the nth iteration, $\mathbf{G}_n$ is:

$$\mathbf{G}_n(\mathbf{s},\mathbf{r},\tau=GA,\alpha\neq0)=\Gamma\Delta\Omega(\mathbf{r})\left\{(\rho_v-\rho_w)v\left(R_{sf}+\frac{b_{n-1}(\mathbf{r})}{2},\psi_{sr}\right)+\frac{(\rho_v-\rho_w)R_{sf}^2}{\pi(\rho_m-\rho_s)\alpha^2}\sum_{\mathbf{r}'\in S}\Delta\Omega(\mathbf{r}')\,\mathrm{Kei}\left(\sqrt{2}\frac{|\mathbf{r}-\mathbf{r}'|}{\alpha}\right)\right.$$

$$\left.\times\left[(\rho_s-\rho_2)v\left(R_{sf}+\frac{w_{n-1}(\mathbf{r}')}{2},\psi_{rr'}\right)+(\rho_2-\rho_3)v\left(R_{2/3}+\frac{w_{n-1}(\mathbf{r}')}{2},\psi_{rr'}\right)+(\rho_3-\rho_m)v\left(R_m+\frac{w_{n-1}(\mathbf{r}')}{2},\psi_{rr'}\right)\right]\right\} \tag{9}$$

with

$$v(R,\psi)=\frac{(a-R)R^2}{\sqrt{a^2+R^2-2aR\cos\psi}^3}. \tag{10}$$

For a datum of gravity anomaly, in context of local compensation and at the nth iteration, $\mathbf{G}_n$ is:

$$\mathbf{G}_n(\mathbf{s},\mathbf{r},\tau=GA,\alpha=0)=\Gamma\Delta\Omega(\mathbf{r})(\rho_v-\rho_w)\left[v\left(R_{sf}+\frac{b_{n-1}(\mathbf{r})}{2},\psi_{sr}\right)-v\left(R_m+\frac{t_{n-1}(\mathbf{r})}{2},\psi_{sr}\right)\right]. \tag{11}$$

2.2 *A priori* information

A priori information has two components: *a priori* values for the model parameters and the covariance of the errors associated with this prior solution. The *a priori* model values for the topography are set to zero. Thus, the covariance matrix of the *a priori* uncertainties should be that of the topography itself, consistently with the kriging/collocation formulations (Moritz 1978; Journel 1989; Herzfeld 1992). Submarine volcanoes are too different in height and slope from one another for a realistic covariance functions to be arrived at on the basis of well-mapped volcanoes, and be used for the computation of the *a priori* covariance of unknown features (non-stationarity). The use of various usual analytic covariance functions has thus been tested (Gauss's, exponenital, 2nd and 3rd Markov's, Damped Cosine, Bessel's, Hirvonen's). After tries with all these, Hirvonen's function appears to be a good candidate since it has a null derivative at the origin, is 'bell shaped' and is robust and computed at low CPU cost. This covariance function is given by:

$$\mathbf{C}_{rr'} = \frac{\sigma_0^2}{1 + [\psi_{rr'}/L_c]^2} \tag{12}$$

where L_c is the correlation length (angular distance of half correlation) and σ_0, the *a priori* uncertainty. The actual values of these parameters are unknown. They can be approached by those given by the covariance function of the *a posteriori* topography issued of a computation with test realistic values. The refined values (which may include a correlation length that varies with azimuth, see Appendix 5), are further entered for a subsequent computation. The effect of the values selected for the correlation length and the auto-covariance is discussed more extensively below within the simulations.

3 SIMULATIONS AND ERROR ANALYSIS

Simulations have been performed to quantify the errors in topography that results from the presented inverse modelling. These errors can be generated by the linearization of the data functionals, the uncertainties associated with the data, the geometry of the data sampling, the use of different *a priori* information and the approximate values used for the geophysical parameters such as the plate stiffness and the volcano density. The data set used to perform the simulations is the following: a volcano topography has been generated as a 0.4° long and 0.3° wide, 2 km high bell-shaped surface at the centre of a $1.25° \times 1.25°$ surface. This surface is divided in 625 nodes ($0.05° \times 0.05°$ grid steps) and is set at the reference depth of 4500 m. It is displayed in Fig. 2(a). Based on this topography, a geoid grid (Fig. 2b) and a gravity anomalies grid (Fig. 2c) have been computed. Table 2 gives the value of all the geophysical parameters used to compute these reference data sets. Value series have been extracted from these grids to simulate satellite tracks for the geoid data and ship courses for the topography and gravity anomalies (shaded bins in Fig. 2). To better simulate true data, some experiments have also been conducted with noise added to the synthetic geoid, gravity anomalies and bathymetry, using a pseudo-random numbers generator. 5 cm, 10 cm and 20 cm additional white noise have been used for the geoid, 6 mGal and 15 mGal for the gravity anomalies and 10 m for the bathymetry.

3.1 Errors due to the linear approximation of the data functionals

The errors in computed topography due to the linearization have been evaluated when the reference geoid and gravity anomaly grids are used as input data (Fig. 3). When inverting the geoid grid, the extreme error is, after a few iterations, less than 20 m and the rms is less than 2 m. As far as the gravity anomalies are concerned, the results are 40 m of maximum error and 5 m rms. According to these results, the linearization does not introduce significant errors in the modelling. The results of the first iteration step are those that a linear hypothesis (instead of iteratively linearizable) would have provided. One can see that in this case, the errors remain significant since the rms error is greater than 30 m using geoid heights and 60 m using gravity anomalies, and the maximum error is close to 400 m for geoid heights and more than 700 m for gravity anomalies. The fact that the linearization induces more errors for gravity anomalies than the geoid heights is consistent with the fact that geoid heights vary more slowly with depth ($1/r$) than gravity anomalies do ($1/r^2$). These two experiments have been conducted with an *a priori* correlation L_c of 0.2° and an *a priori* uncertainty σ_0 of 1000 m. In these cases, the true values of L_c are not critical and identical results have been reached with other realistic values (0.001°, 0.1° and 0.3°). However, results are not that good with smaller values for σ_0, but the value of 1000 m is nevertheless retained because it corresponds to a weak *a priori* information and subsequently to an *a posteriori* model mainly constrained by the data information, which is the way to analyse the accuracy of the linear approximation of the data functionals.

3.2 Errors associated with the *a priori* information

When the data coverage is not that dense, the covariance function used for *a priori* information is of greater importance. The larger the L_c is, the further the correlation extends and the better the partly resolved model parameters seem to be resolved.

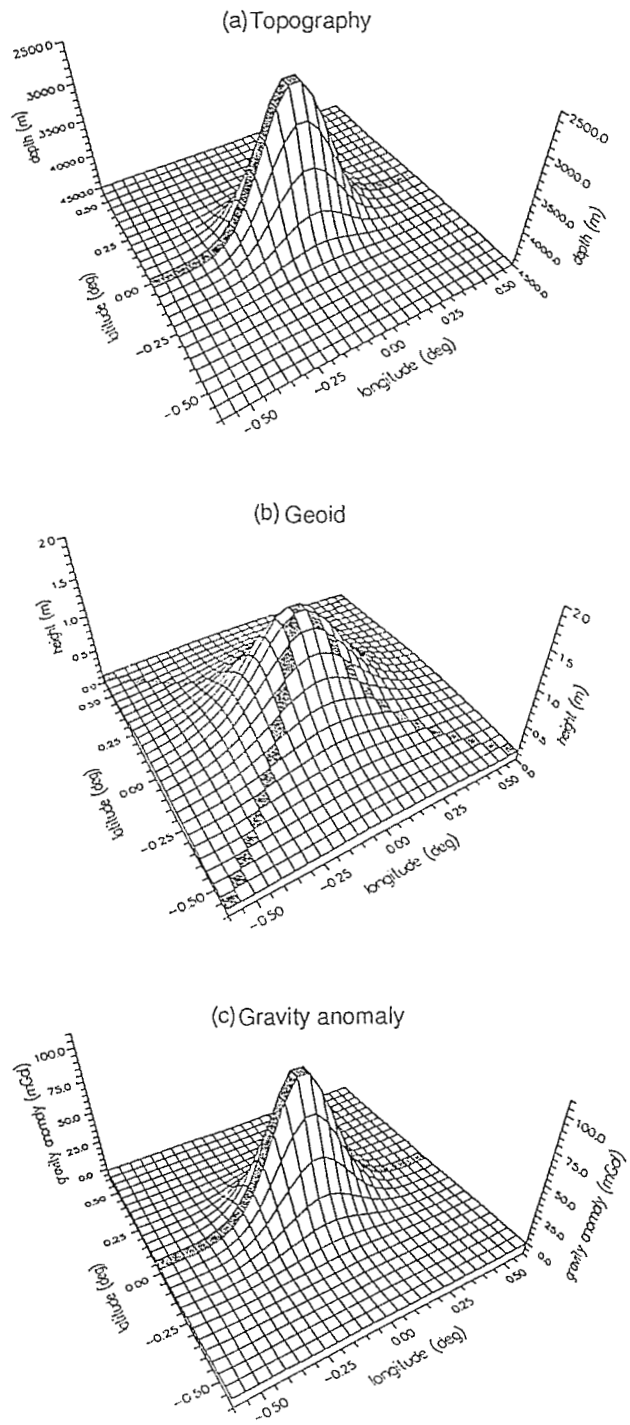

Figure 2. Simulated data. The grid is 1.25° × 1.25° wide and the grid step is 0.05° (i.e. 625 grid points). (a) Topography of the seamount (2000 m high, lying over a 4500 m reference depth), further used as reference topography. (b) Geoidal signature over the same grid. The maximum height of the geoid anomaly is 1.7 m (c) Gravity anomaly due to the seamount over the grid. The maximum value is 100 mGal. (b) and (c) are computed with the reference values given in Table 1. The values extracted from these gridded sets to simulate geoid undulation measurements from a satellite altimeter and a shipborne profile of bathymetry and gravity anomalies are shaded.

This effect is shown in Fig. 4. The results presented in this figure have been obtained by using as input data two geoid tracks extracted from the reference geoid grid. The best results are obtained with $L_c = 0.2°$. This L_c value is close to the values of the true correlation lengths (the simulated structure is not isotropic, see Fig. 5).

The value taken for the *a priori* uncertainty also affects the solution. The true variance of the studied topography, square of the uncertainty, should be used in agreement with a collocation/kriging point of view. Besides, the larger the *a priori* uncertainty, the closer the solution will fit the data and the lesser the constraint on the solution from a parameter altogether

Table 2. Numerical value of geophysical parameters used in the simulations.

volcano density	2.6 10^3 kg/m^3
density of sediments	2.6 10^3 kg/m^3
density of crustal layer 2	2.7 10^3 kg/m^3
density of crustal layer 3	2.9 10^3 kg/m^3
density of upper mantle	3.35 10^3 kg/m^3
flexural rigidity	7. 10^{22} Nm
seafloor depth	4500 m
thickness of layer 2	2500 m
thickness of layer 3	4000 m

unknown. The errors associated with the use of different values of σ_0 are shown in Fig. 6. The rms errors between the reference seamount and the computed solution (model space) are shown in Fig. 6(a) and the rms errors between the geoid data and the geoid heights computed from the *a posteriori* model (data space) are shown in Fig. 6(b). This data set comprises two tracks extracted from the reference-simulated geoid heights to which a noise of 5 cm has been added. These simulations have been performed using $L_c = 0.2°$. In the model space, the best agreement between the reference and computed topographies is achieved when using $\sigma_0 = 350$ m. This value of *a priori* uncertainty corresponds to the square root of the auto-covariance of the simulated topography. The worst agreements in the model space are achieved with the extreme values of $\sigma_0 = 4500$ m (the sea-floor depth) and $\sigma_0 = 100$ m. The results in the data space show that these values correspond to inadequate information. For $\sigma_0 = 4500$ m, this large value corresponds to a very weak *a priori* constraint on the solution. The geoidal signature of the posterior topography obtained using this value of σ_0 approaches the data values better than the data uncertainty (1.5 cm rms

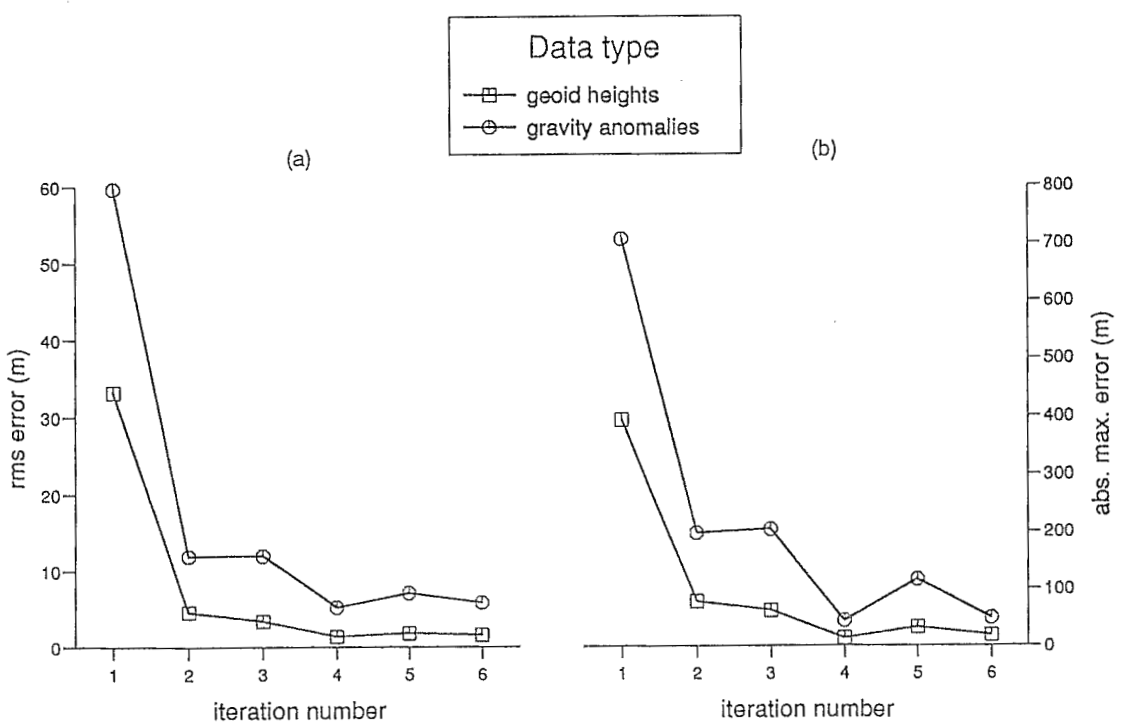

Figure 3. Errors due to the linearization scheme for geoid heights and for gravity anomalies. The errors are computed as the difference between the *a posteriori* solution and the reference topography. The rms difference (a) and the extreme absolute difference (b) are shown.

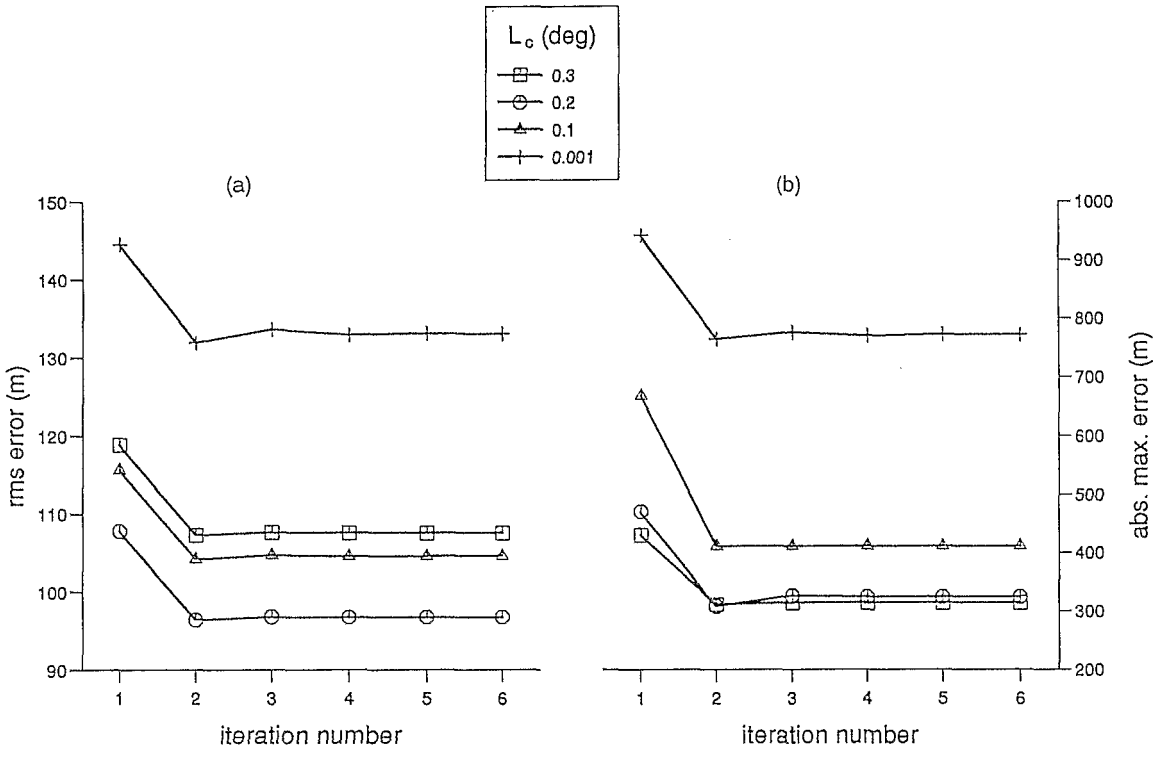

Figure 4. Errors related to the value of the correlation length L_c used in the *a priori* information. The errors are computed as the difference between the *a posteriori* solution and the reference topography. The rms difference (a) and the extreme absolute difference (b) are shown. The data set used is made up of the two geoid tracks with 5 cm (rms) noise added.

difference instead of 5 cm for the data uncertainty). Conversely, the small value of $\sigma_0 = 100$ m restraints the solution too closely to the *a priori* value and the rms difference in the data space is larger (7.3 cm) that the data uncertainty.

The *a posteriori* solutions have an auto-covariance intermediate between the one entered in *a priori* and the actual one (mean $L_c = 0.2$ and $\sigma_0 = 330$ m). From 30 tests computed with L_c values of 0.001°, 0.1°, 0.25°, 0.35° and 0.5°, and σ_0 values of 100 m, 350 m, 500 m, 1000 m, 2500 m and 4500 m, it appears out that the value of L_c for the auto-covariance of the *a posteriori* solution lies within 0.15° and 0.24°, and that the value of the variance lies within 250 m and 400 m. Clearly, these two parameters can thus be adjusted in two or three runs in order to largely reduce the errors previously pointed out. This step is also important when dealing with the *a posteriori* uncertainties. According to eq. (3), these are strongly related to the *a priori*

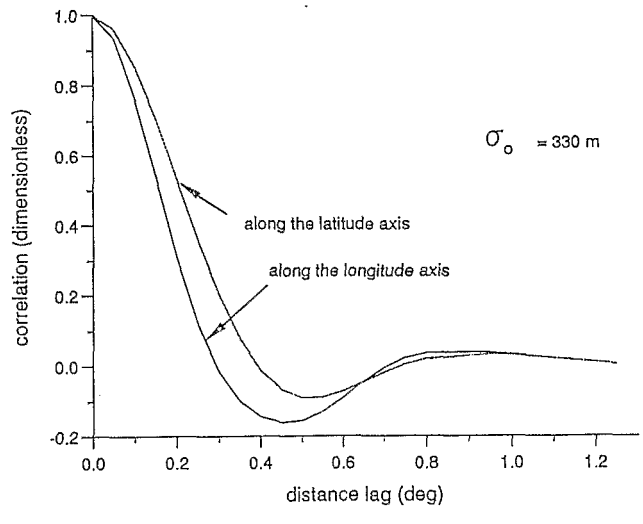

Figure 5. Auto-covariance of the reference topography. The auto-correlation (auto-covariance normalized by its variance) is displayed and the square root of the variance, σ_0, is indicated. The two curves stand for the correlation along the longitude and latitude axes, pointing out the slight anisotropy present in the reference topography.

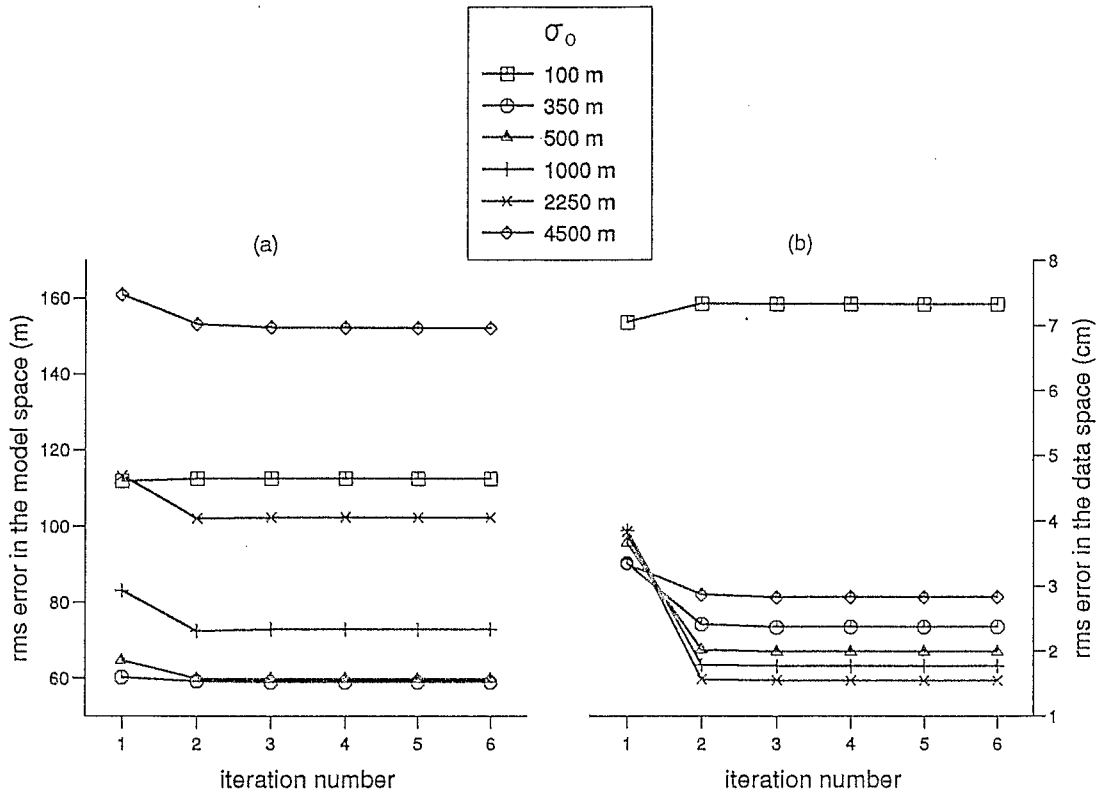

Figure 6. Errors related to the value of the uncertainty used in the *a priori* information. The errors are computed as the difference between the *a posteriori* solution and the reference topography. The rms difference (a) and the extreme absolute difference (b) are shown. The data set used is made of the two geoid tracks with 5 cm (rms) noise added.

covariance and are upper bounded by the *a priori* uncertainty σ_0. Thus, realistic *a posteriori* uncertainties require that the *a priori* covariance function be finely determined by iterative fitting.

3.3 Errors due to the data uncertainties

The model parameters produced by the inversions also depends on the error function of the data. As far as geoid heights are concerned, the data errors may be restricted to two sources. First are the measurement errors that can be modelled by a Dirac function. Second is a long-wavelength error. The gravitational signature of the volcanoes only represent the short wavelength part of the geoid heights. Even when removing a long-wavelength reference field to the data and performing a cross-over adjustment, all the long wavelengths unrelated to the current problem cannot be exactly removed and it has to be accounted in the budget of data errors. For gravity anomalies and bathymetric data, only the measurement errors have been considered.

The results of the simulations relating to the measurement errors are presented in Fig. 7 for the data sets of the geoid and gravity anomalies. For these simulations, the measurement errors consist of a random value within different bounds added to the data simulating a white noise. The bounds are 5 cm, 10 cm and 20 cm for the geoid data and 6 mGal and 15 mGal for the gravity data. 5 cm are representative of data from Geosat, ERS-1 and Topex/Poséïdon, 10 cm for Seasat and 20 cm for Geos-3 (Sailor & LeSchack 1987). 6 mGal and 15 mGal are for shipborne data of good and bad quality respectively. The base data sets are the reference grids. They show that good results may be expected with the recent satellites even with data from Geos-3 (not taking into account the numerous spikes present in this data set). When measurement noise is as large as 10 cm, no improvement can be obtained by iteration. As far as the gravity anomalies are concerned, good results are still obtained with a 6 mGal measurement error but 15 mGal seems to be the upper limit of usable data since errors remain large and are not improved by iterations.

The other important source of error in the geoid data is the presence of a long-wavelength signal unrelated to the volcano gravitational signature. This case has been simulated by removing a constant bias of the two geoid tracks extracted from the reference geoid grid. When this geoid data set is used alone, the errors (reference topography minus *a posteriori* topography) appear as a 2-D undulation over the grid (Fig. 8a): the errors are rather low for the well-resolved model points (along the data tracks) but the few resolved grid points present well-pronounced topographic lows. Indeed, the central topographic high

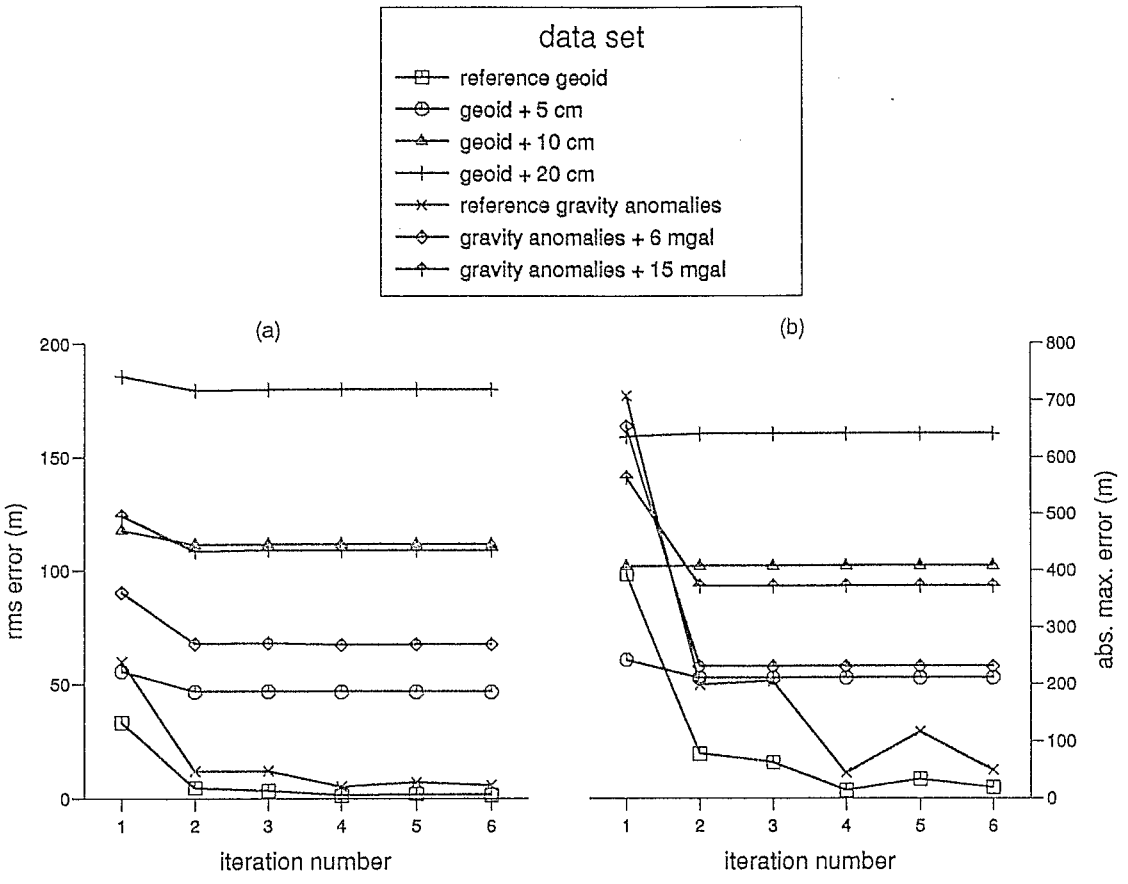

Figure 7. Errors related to the data-measurement uncertainties, computed as the difference between the *a posteriori* solution and the reference topography. The rms difference (a) and the extreme absolute difference (b) are shown. The data set used are the geoid and gravity grids with white noise added. For geoid height measurements, an additional noise of 5 cm simulates measurements from the Geosat, ERS-1 and Topex/Poséïdon altimeters, 10 cm is used for Seasat and 20 cm for Geos-3. For gravity-anomaly measurements, 6 mGal and 15 mGal stand for respectively good- and bad-quality data.

generates positive geoid heights all along the data tracks and the topographic lows are necessary to provide the negative data values at the boundaries of the grid. Although the overall height of the seamount is correctly restored, this result is not satisfactory since *a posteriori* values far from the *a priori* solution for few resolved model parameters are characteristic of an inconsistency between the data set and the linear operator. When a bathymetric track is added to the data set (see Fig. 2 for location), the errors for the few resolved model points are even larger (Figs 8c and d) and the global rms error is increased: 510 m in cases (c)–(d) instead of 460 m in cases (a)–(b). This must be due to a second inconsistency between the two sets of data.

It thus appears necessary to account for such an error in the data covariance matrix. It has been introduced as a Gaussian covariance of variance $= (-0.3\text{ m})^2$ and correlation length much larger than the size of the studied area. It has been applied to all the geoid height data in a simulation identical to that presented in case 8(c), the result of which is shown in Fig. 8(e). The overall error is greatly reduced (rms of 33 m, see Fig. 8f). All the model points have low errors whether they are well resolved or not. The inconsistency that was previously accommodated by the model points mostly constrained by the only *a priori* information is then properly accounted for by the introduction of this long wavelength in the data covariance matrix. It must be noted that when geoid heights are the only available data type, entering such a long-wavelength covariance may make the sum matrix in eq. (1) improper for inversion. The best way to handle this problem is a trail method, adding different constant values to the geoid heights until the undulation is minimum. This procedure requires that the data set is selected in such a way that some model parameters remain unresolved in order that the inconsistency can be highlighted.

3.4 Errors associated with the geophysical parameters

Simulations have also been performed in order to test the effect of non-exact values for the geophysical parameters such as the lithospheric stiffness or the volcano density. These simulations have been performed with $\sigma_0 = 1000$ m and $L_c = 0.2°$. The data

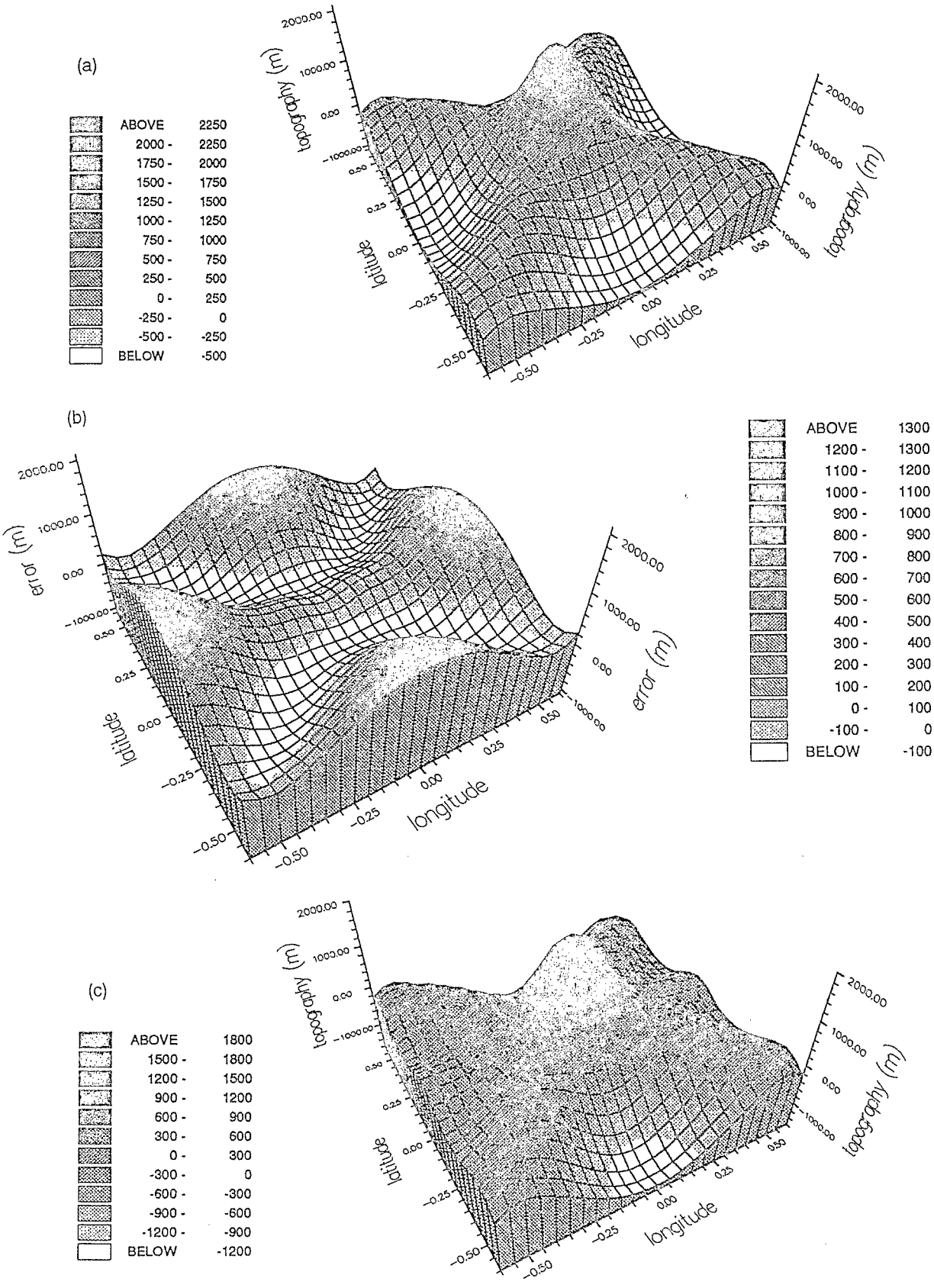

Figure 8. Errors related to the removal of the long wavelengths in the total geoid signal to extract the short-wavelength signal related to the volcanic feature. It is simulated by subtracting 30 cm to all the data values of the two geoid tracks. (a) *A posteriori* topography. (b) Errors, computed as the difference between the reference topography and the *a posteriori* topography in (a). That the data kernel and data values are no longer consistent are highlighted by the *a posteriori* values for the grid points far from the data. For these poorly resolved model parameters, the *a posteriori* values should be close to the *a priori* values, i.e. close to zero. (c) Modelled topography when the bathymetric profile is added. (d) Errors of the topography in (c). The errors are larger than in case (b) although more data are used. When the bias uncertainty is accounted for in the data-error covariance matrix, the erroneous topography undulation present in the previous simulations doesn't exist anymore, (e) and the errors are greatly reduced (f).

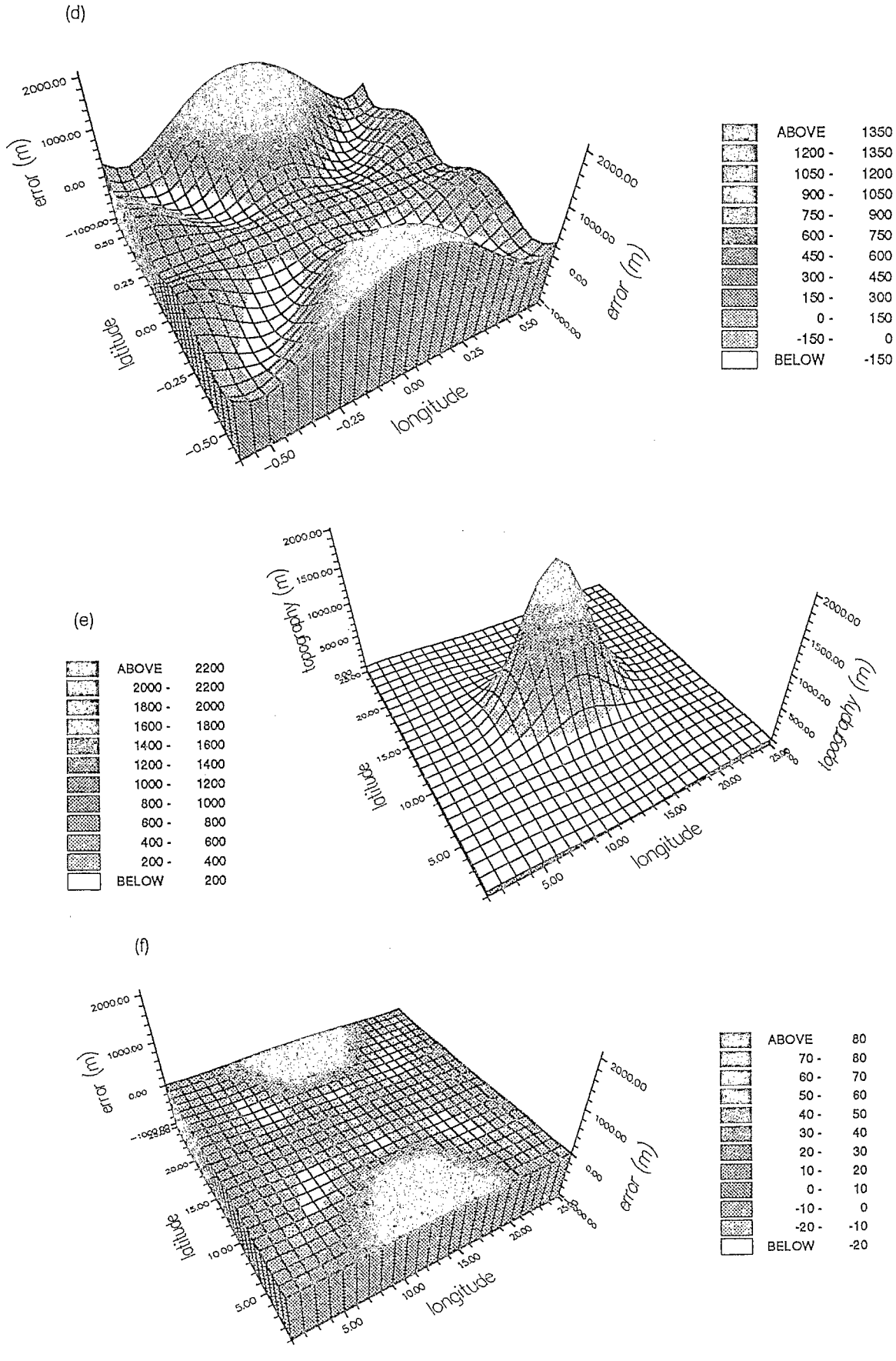

Figure 8. (*Continued*).

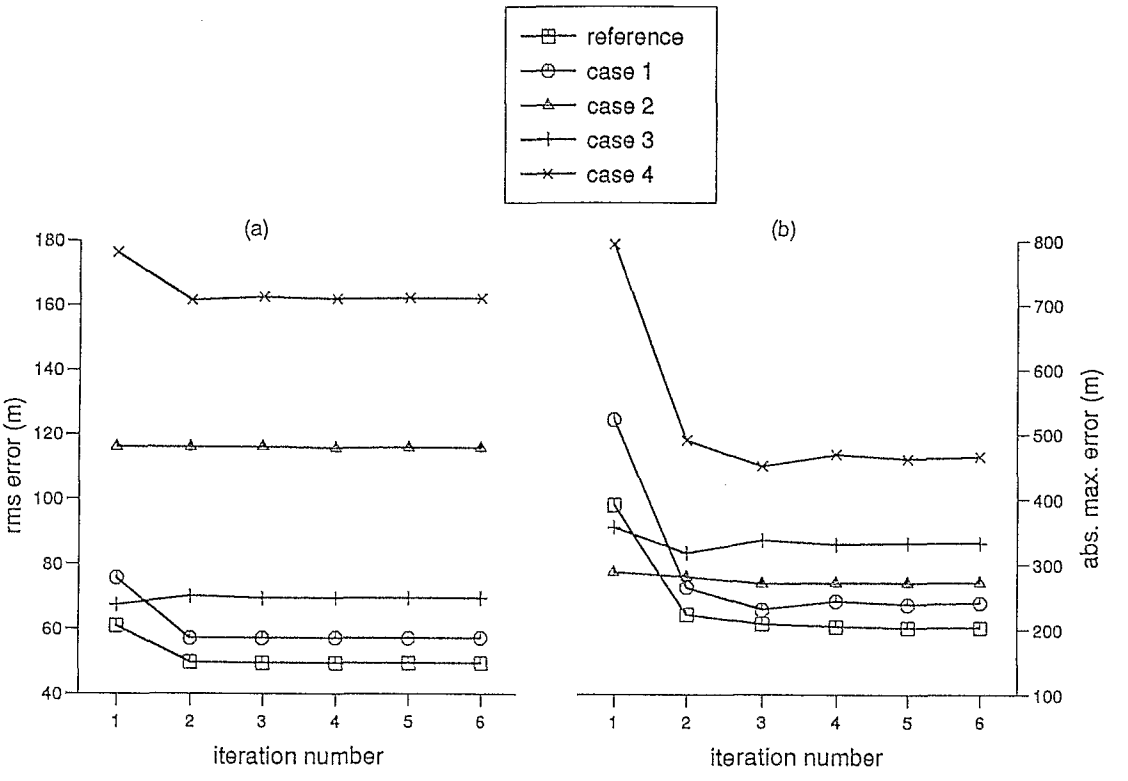

Figure 9. Errors related to the value of the geophysical parameters used to compute the data functional and the linear operators. Two parameters are considered: the plate stiffness D and the volcano density ρ_v. The four cases correspond to the following values:

case 1: $D = 1.5\,10^{23}$ Nm and $\rho_v = 2.5\,\mathrm{g\,cm^{-3}}$
$D > D_{\mathrm{ref}}$ and $\rho_v < \rho_{v,\mathrm{ref}}$.
case 2: $D = 1.0\,10^{22}$ Nm and $\rho_v = 2.8\,\mathrm{g\,cm^{-3}}$.
$D < D_{\mathrm{ref}}$ and $\rho_v > \rho_{v,\mathrm{ref}}$.
case 3: $D = 1.5\,10^{23}$ Nm and $\rho_v = 2.8\,\mathrm{g\,cm^{-3}}$.
$D > D_{\mathrm{ref}}$ and $\rho_v > \rho_{v,\mathrm{ref}}$.
case 4: $D = 1.0\,10^{22}$ Nm and $\rho_v = 2.5\,\mathrm{g\,cm^{-3}}$.
$D < D_{\mathrm{ref}}$ and $\rho_v < \rho_{v,\mathrm{ref}}$.

The errors are computed as the difference between the *a posteriori* solution and the reference topography. The rms difference (a) and the extreme absolute difference (b) are shown. The data set used is made of the two geoid tracks (noiseless).

set is the couple of geoid tracks extracted from the reference geoid (no noise added). The various cases, the results of which are shown in Fig. 9, are: for the reference case, a stiffness D of 7.10^{22} Nm and a load density ρ_v of $2.610^3\,\mathrm{kg\,m^{-3}}$; for case 1, an overestimate of D (1.510^{23} Nm) and an underestimate of ρ_v ($2.5\,10^3\,\mathrm{kg\,m^{-3}}$); for case 2 an underestimate of D ($1.0\,10^{22}$ Nm) and an overestimate of ρ_v ($2.8\,10^3\,\mathrm{kg\,m^{-3}}$); for case 3 an overestimate of D ($1.5\,10^{23}$ Nm) and an overestimate of ρ_v ($2.8\,10^3\,\mathrm{kg\,m^{-3}}$); and for case 4 an underestimate of D ($1.0\,10^{22}$ Nm) and an underestimate of ρ_v ($2.5\,10^3\,\mathrm{kg\,m^{-3}}$). The lowest errors are obtained in case 1 and the largest errors in case 4. Indeed, the stiffness and the load density act in opposite ways: the larger the load density, the smaller the volume needed to produce a given gravitational signature and the larger the assumed stiffness for the lithosphere, the larger the plate deflection and volume of the negative density contrasts within the plate and the larger the load to produce the observed signature. In addition, the *a posteriori* model is less sensitive to wrong estimates of the stiffness than those of the load density. In any case, it seems better to overestimate the stiffness than to underestimate it and, consequently, to slightly underestimate the load density if not well known.

3.5 Simulation of a realistic case

Finally, the results of a simulation in a realistic case are shown in Fig. 10. In this case, the model parameters are computed using the reference geoid grid, undersampled to one data point every 10 km with 5 cm white noise added; the stiffness and load density are assumed to be $D = 10^{23}$ Nm (overestimated) and $\rho_v = 2.5\,10^3\,\mathrm{kg\,m^{-3}}$ (underestimated), respectively; the *a priori* information is $L_c = 0.3°$ and $\sigma_0 = 500$ m. The *a posteriori* seamount topography illustrated in Fig. 10(a) is clearly a good result since the rms of the errors (difference between reference and computed topographies) is less than 50 m. Indeed, when a profile

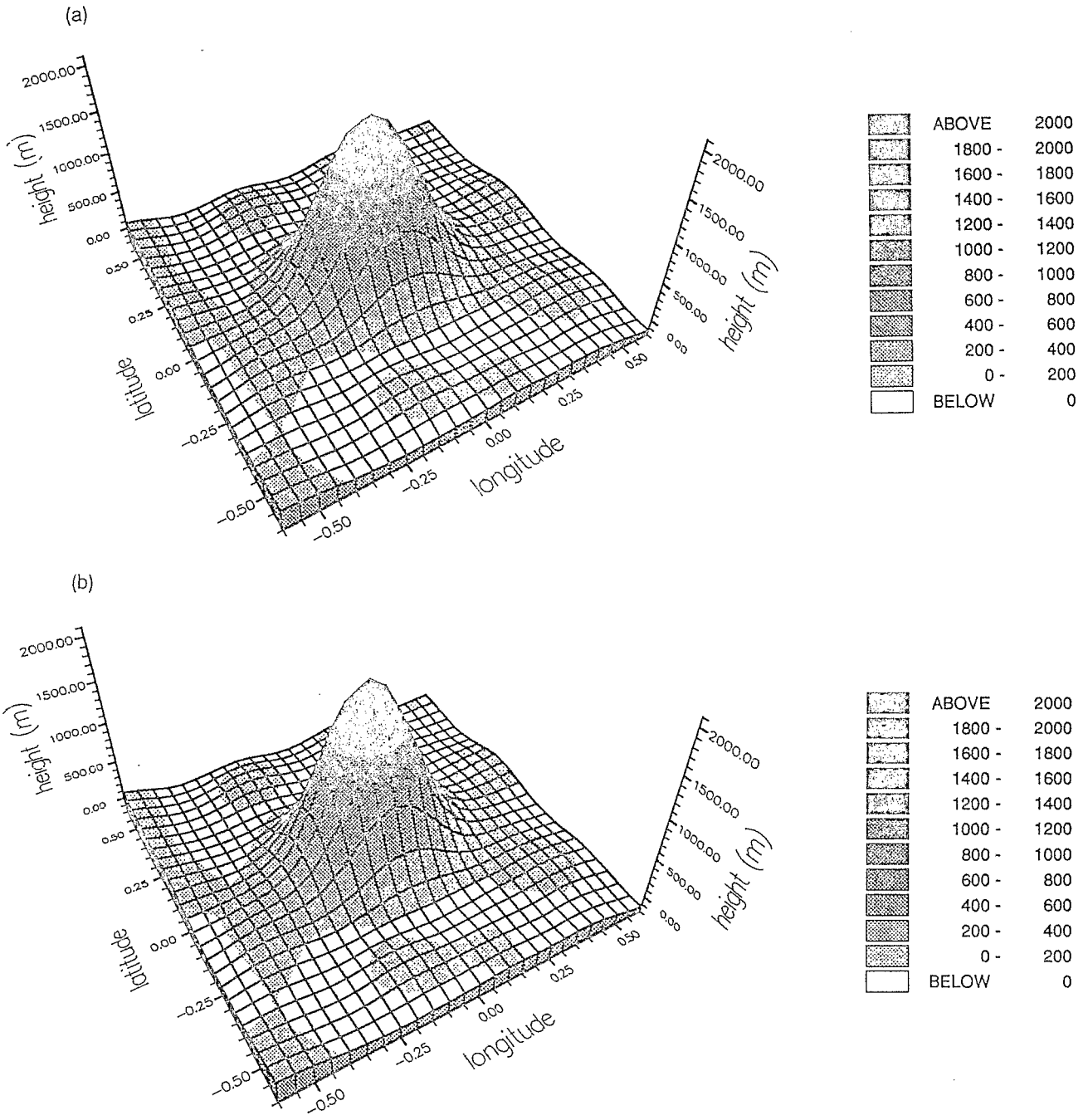

Figure 10. Example of *a posteriori* topography in a realistic case (the computation is made with slightly wrong values for the parameters, which should be unknown: $D = 10^{23}$ Nm, $\rho_c = 2.5\,\mathrm{g\,cm^{-3}}$, $L_c = 0.3°$, $\sigma_0 = 500$ m). In (a) the data set used is the geoid grid undersampled at one data point every two grid points in both directions. A 5 cm white noise is added to the data values. The rms error is 46 m. In (b) the profiles of bathymetry and gravity anomalies are added to the previous data set. The rms error is 43 m.

of bathymetry and gravity anomalies is added to the data set, there is no significant improvement of the overall errors (see Fig. 10b). Posterior uncertainties are shown in Fig. 11 for solutions using geoid heights only (Fig. 11a) and with the addition of the profiles of the bathymetry and gravity anomalies (Fig. 11b). They vary from 69 to 170 m in the first case and from 13 to 170 m when the profiles are added. The largest values occur at the grid boundary. If these grid points are omitted, the largest uncertainties are 80 m in both cases. The posterior uncertainties obtained when using the geoid heights and the bathymetric and gravimetric profiles are compared to the actual errors in Fig. 12. The uncertainties are larger than the errors for 95 per cent of the grid points, and only four grid points out of 625 present an error twice as large as the computed uncertainty. This result means that all the components that enter into the computation of these uncertainties are properly taken into account.

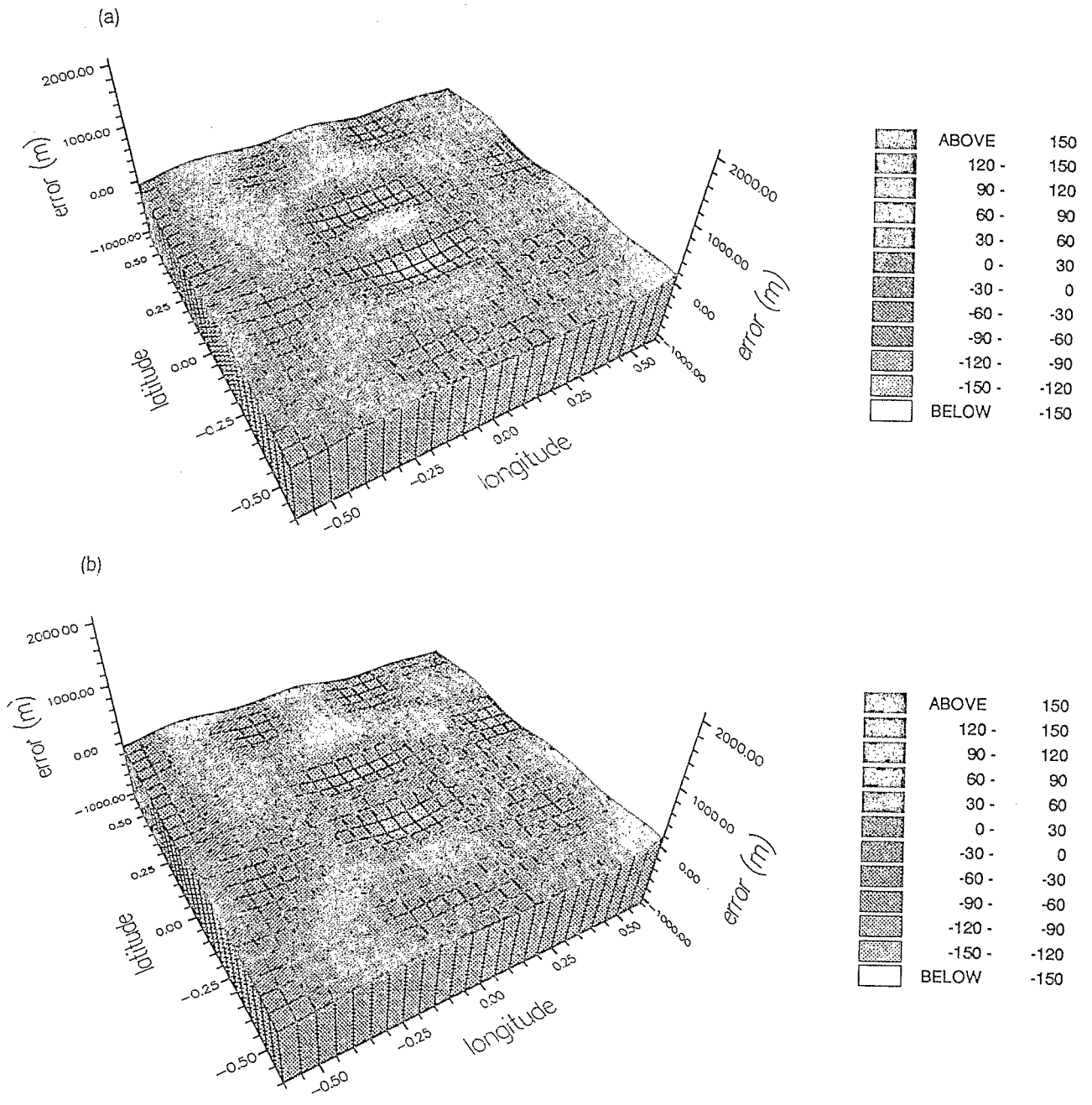

Figure 11. *A posteriori* uncertainties associated with the topographies in Fig. 10.

These components are the data kernel, the spatial distribution of the data, their error functions and the *a priori* information. In actual practice, this last term is the most difficult to adjust. Indeed, if the studied feature is far too irregular as regards the data coverage (high energy at unsampled wavelengths), the selected covariance function is not adequate and significant errors occur that cannot be handled even iteratively. This point is elaborated upon in the following chapter, which addresses the study of a seamount already surveyed.

4 CASE STUDY

S6 is a seamount in French Polynesia, South Pacific, which was first detected using altimetric data (Sandwell 1984). The seamount location proposed in that study was about 35 km south of the actual one and a more precise determination was given by Baudry *et al.* (1987). A shipboard confirmation was performed during the SEAPSO-5 cruise aboard the R/V Jean-Charcot

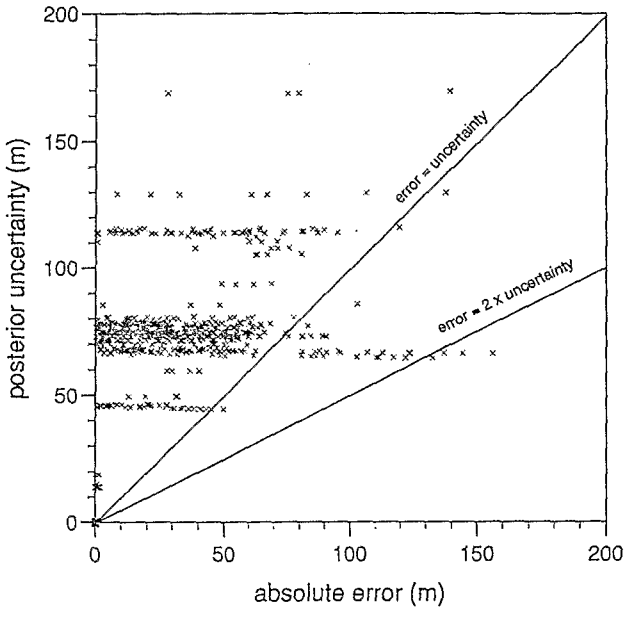

Figure 12. Posteriori uncertainties (case 10b) versus error relative to the reference topography.

(Baudry & Diament 1987). The topography of this seamount has been modelled by Baudry & Calmant (1991) using Fourier Transforms to convert the geoid grid into a bathymetric grid. This seamount has two well-differentiated peaks and consequently it is noticeably different from the somewhat idealized seamount previously used for the simulations. Last, the two Seasat tracks used in this study pass over the peaks and the central saddle is not sampled.

The grid used for the definition of the model parameters is $1.3° \times 1.3°$ large, centred at 24.1°S of latitude and 203.7°W of longitude, and the grid step is 0.05° in both directions (i.e. 728 bins). The data set available over this seamount comprises a pair of Seasat tracks that each pass over one peak, and a shipborne profile of bathymetry and gravity anomalies from SEAPSO-5. For the purpose of this study the bathymetric and gravimetric profiles have been binned according to the grid, the average of the data over each grid element providing the data set and the associated variances providing the corresponding data uncertainty (Figs 13a and b). This bathymetric profile is further used to test the computed topography. The values used for the computations are $D = 10^{21}$ Nm and $\rho_v = 2.6\,10^3\,\mathrm{kg\,m^{-3}}$ for the flexural rigidity and the load density, respectively. The crustal model is: layer 2 with a thickness of 2.5 km and a density of $2.6\,10^3\,\mathrm{kg\,m^{-3}}$ and a layer 3 with a thickness of 5 km and a density of $2.9\,10^3\,\mathrm{kg\,m^{-3}}$; the mantle density is $3.35\,10^3\,\mathrm{kg\,m^{-3}}$. Fig. 14 illustrates the seamount topography computed using: (a) the altimetric data, (b) the discretized gravity anomalies, and (c) all the data; along a roughly east–west-trending profile (this profile does not cross the summits). These solutions have been reached by iteratively adjusting the *a priori* covariance function. The final values are $L_c = 0.2°$ (no anisotropy could be clearly pointed out) and $\sigma_0 = 400$ m. The data have been bias adjusted in the altimetric solution so as to minimize the artefacts described in Section 3.3, and in the complete solution a long-wavelength error of 0.2 m in amplitude has been accounted for in the error function associated with the altimetric data.

The altimetric solution (a) appears slightly less accurate than the gravimetric solution (b) since the rms error in (a) is 46 m compared to 43 m in (b). However, the displayed values correspond to more poorly resolved grid points for solution (a) than for (b) and thus to grid points where the solution is more sensitive to the *a priori* information. The largest errors in (a) occur where the actual bathymetry presents noticeable slope variations and the *a priori* covariance function is not able to provide this information. Accordingly, the altimetric data set is not able to resolve the two-peak shape as no topographic low is present at the centre of the computed feature (Fig. 15a). Neither does the gravimetric solution (Fig. 15b), nor the complete solution (Fig. 15c). This is due to the large data uncertainties associated with the binned profiles. These large uncertainties are due to the large standard deviations of the bathymetry within the bins in this area. For the gravity anomalies uncertainties are 6 mGal. Although it is realistic in terms of measurement accuracy, this filters out the high frequencies in the data set. The way to obtain this central low with altimetric data would be to make the computations for smaller discretization steps. This would require denser altimetric data sets. This might be achieved using 10 Hz data of altimetric missions dedicated to dense coverage such as the Geosat Geodetic Mission.

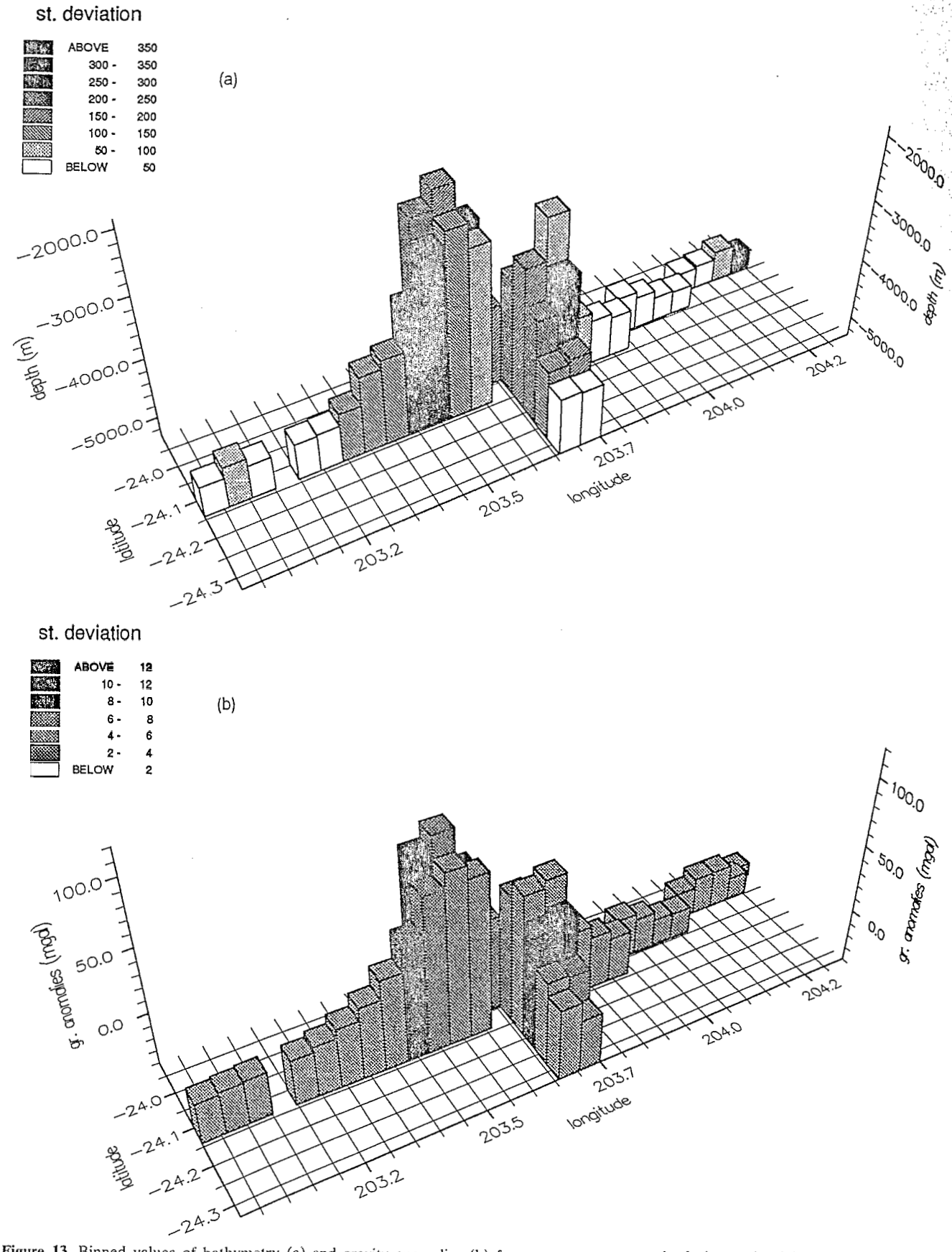

Figure 13. Binned values of bathymetry (a) and gravity anomalies (b) from measurements made during cruise SEAPSO-5 aboard R/V J. Charcot. The shade scale stands for the standard deviation around each mean value, further used as the data uncertainty.

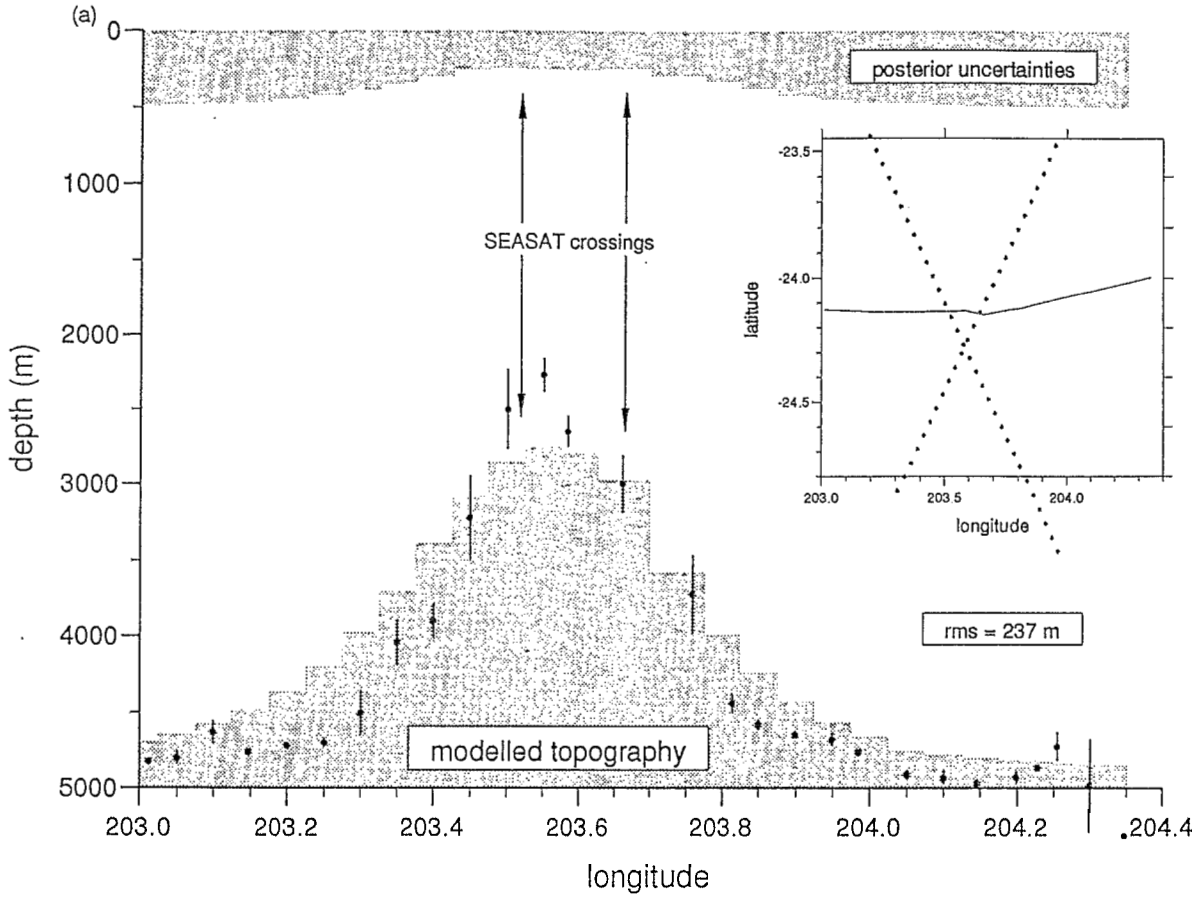

Figure 14. Study of seamount S6. Posterior solution along an E–W-trending profile. The data coordinates (dots) and the location of the displayed profile (line) are given in icon. The shaded areas represent the posterior topography (bottom) and uncertainties (top). The barred dots stand for the binned bathymetry and the associated uncertainty. Crossings between the displayed bathymetric profiles and the Seasat profiles used as data set are indicated. (a) Solution using Seasat data only. Crossings between the displayed bathymetric profiles and the Seasat profiles used as data set are indicated. (b) Solution using binned gravity anomalies from SEAPSO-5. (c) Solution using Seasat data and binned profiles of bathymetry and gravity anomalies from SEAPSO-5 data.

5 CONCLUSION

The presented modelling, based on a least-squares inversion with *a priori* information, is indeed able to provide realistic values for the topography of a submarine volcano from geoid heights, whether or not this data set is completed with bathymetry and/or gravity anomalies data. With Seasat data only, the addition of shipborne data noticeably improves the solution, but when the data set of altimetric geoid heights is dense enough (5 km data spacing could be rapidly available by merging data from the Geodetic Mission of Geosat, Topex/Poséïdon and ERS-1), the bathymetric and gravimetric data will mostly provide a control information about the consistency between the geoid data and the linear operator.

As the parameters of the *a priori* covariance function (variance and correlation length) cannot be accurately defined in advance and since erroenous values may affect the results, these parameters can be iteratively adjusted by comparing the auto-covariance of the *a posteriori* topography with the *a priori* values, within the limits of the wavelengths actually sampled to avoid aliasing effects. When using the dense coverage data to come, the *a priori* information will be less crucial than in the examples presented here.

Using the method presented in this paper, the computation of gridded bathymetric values from all the bathymetric and altimetric data can now be envisaged even on small computers (the present work has been achieved on a workstation with only 32 Mb RAM and each solution took less than one hour to be attained). Bathymetry data are able to restore the long wavelength in the bathymetry. Altimetry data can be converted in short-wavelength bathymetry. A bathymetric grid computed in taking advantage of both data sets would represent a dramatic improvement from the existing bathymetric data bases such as ETOPO-5 (Smith 1993). This work is now conducted on the EEZ of New Caledonia as a part of the French National Program for the valuation of the EEZ of the French Oversea Territories.

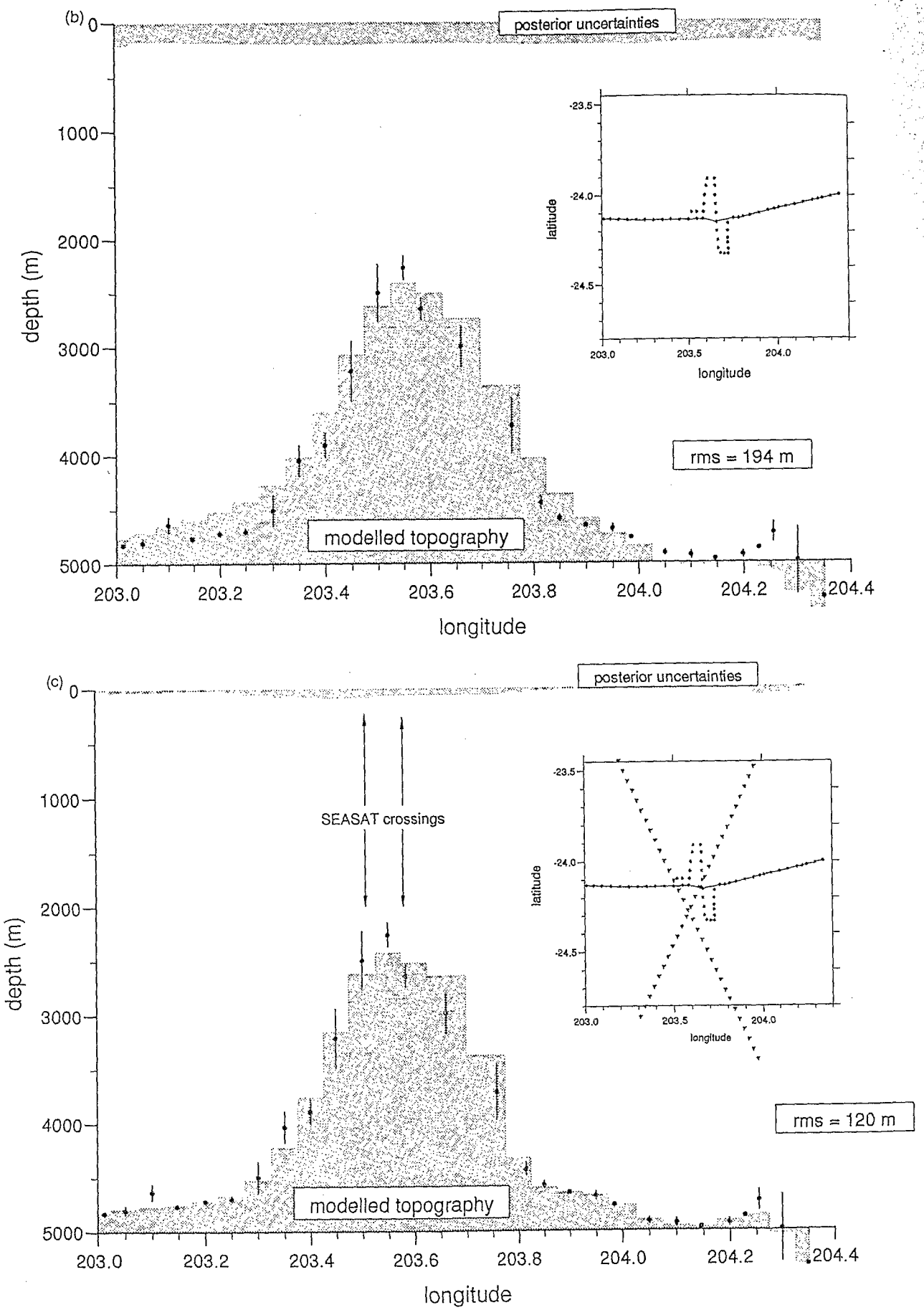

Figure 14. (*Continued*).

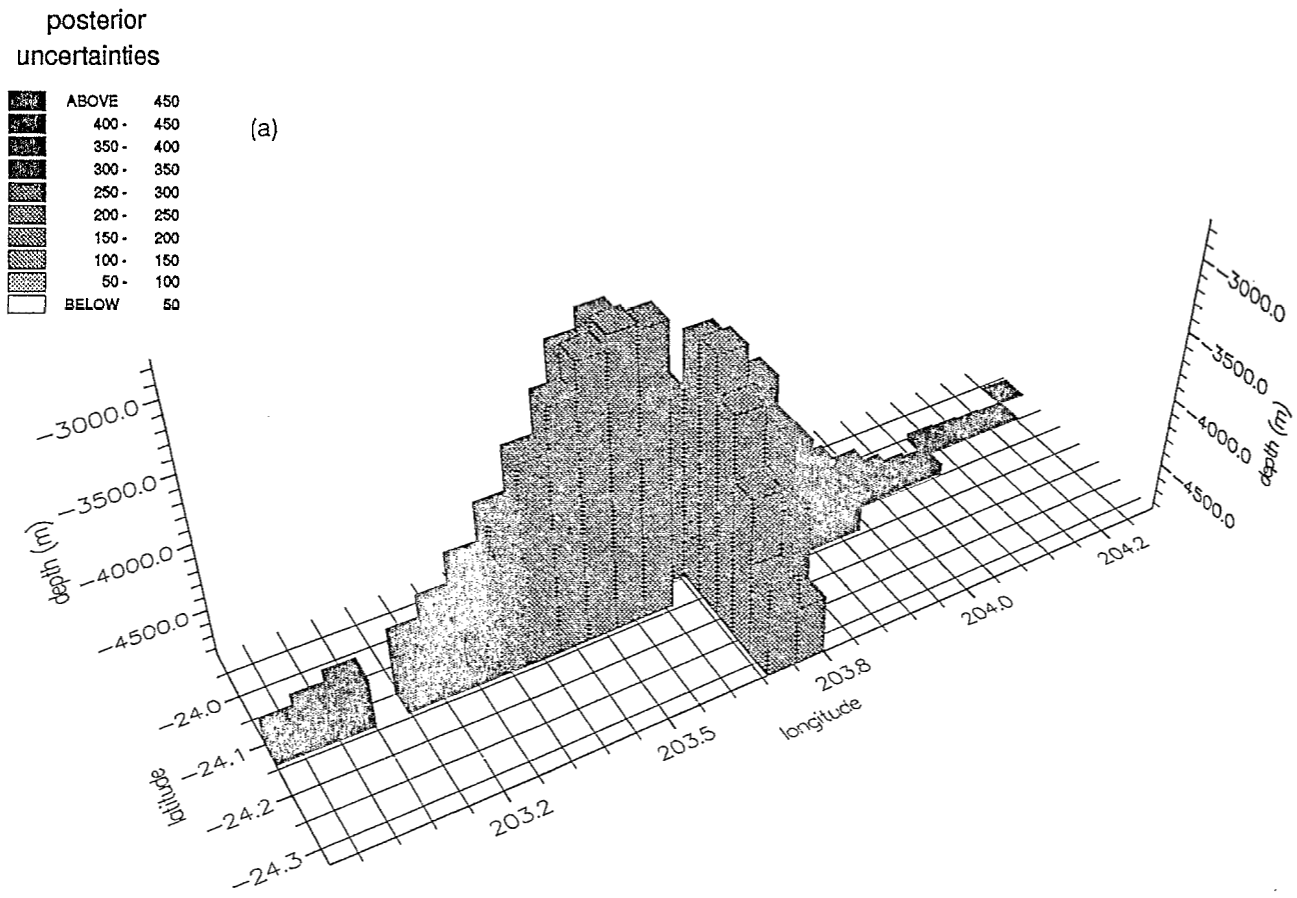

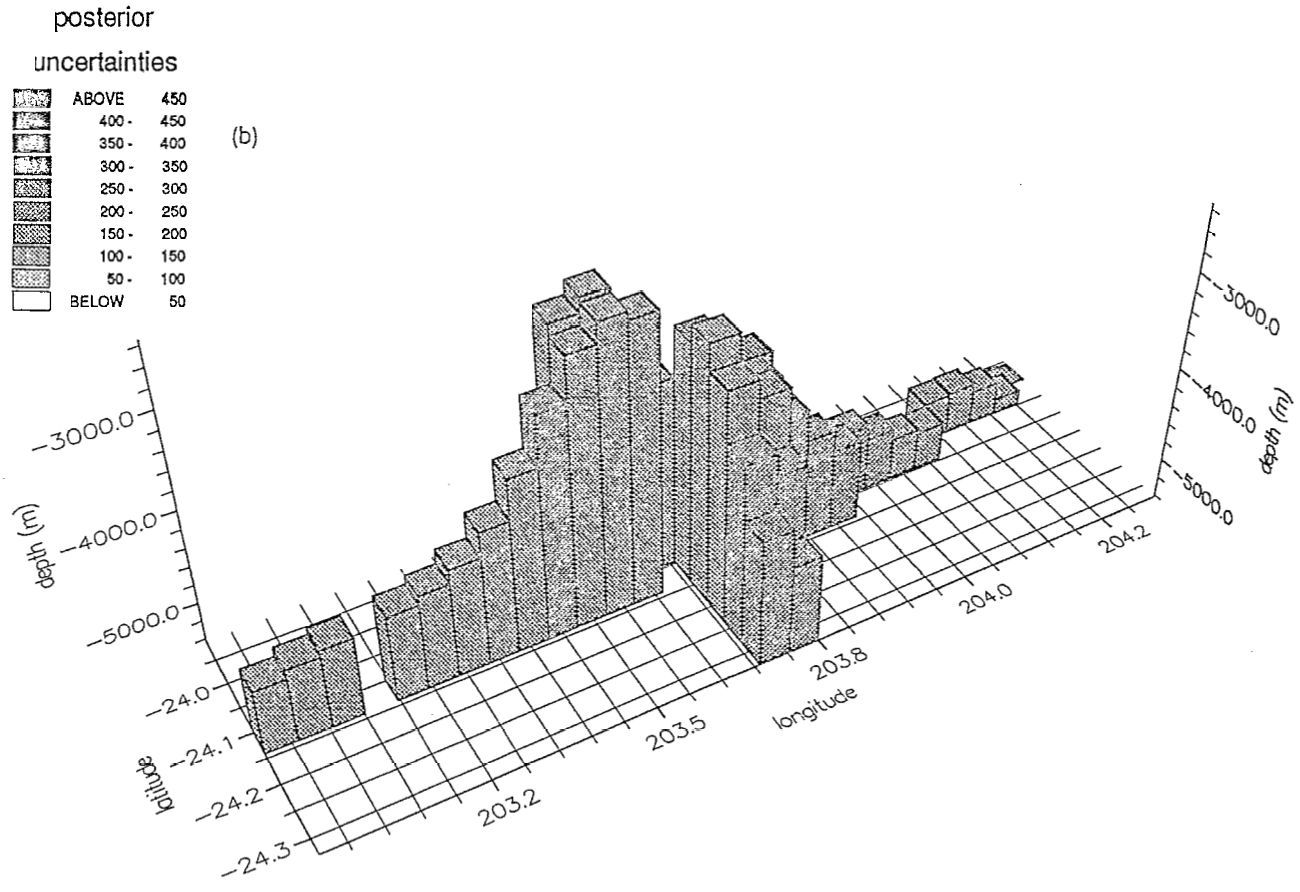

Figure 15. Study of seamount S6. Posterior topography and uncertainties all along the SEAPSO-5 course, showing in particular the computed values at the location of the summits. (a) Solution using Seasat data only. (b) Solution using binned gravity anomalies from SEAPSO-5. (c) Solution using Seasat data and binned profiles of bathymetry and gravity anomalies from SEAPSO-5.

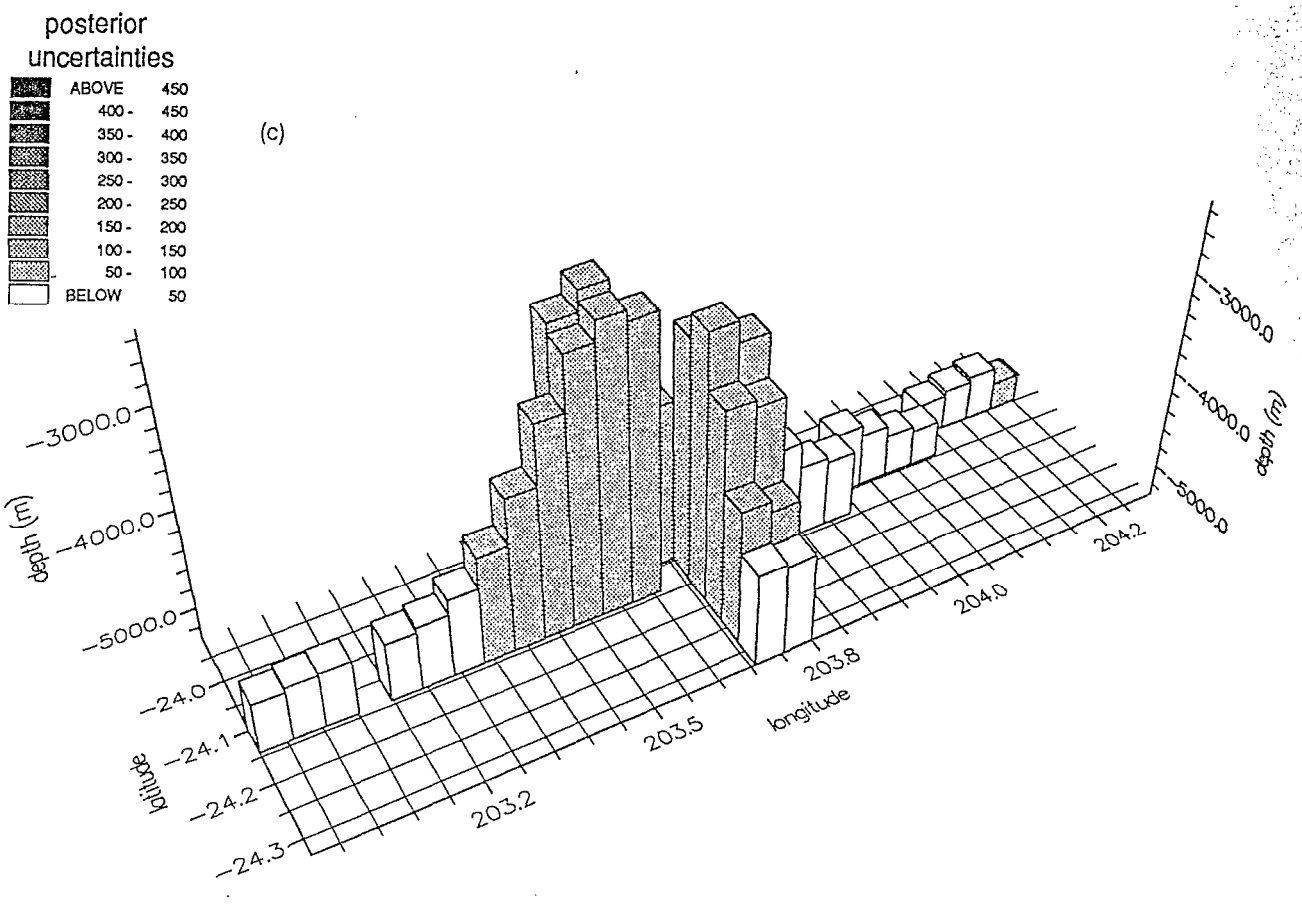

Figure 15. (*Continued*)

ACKNOWLEDGMENTS

P. Mazzega and an anonymous reviewer are greatly acknowledged for their fruitful comments and criticisms on the preliminary version of the manuscript.

REFERENCES

Baudry, N., 1988. Recherche de monts sous-marins non cartographiés en Polynésie Française par l'analyse de données altimétriques satellitaires, in *Conv., Sci Terre, Géol. Géophys.* **3,** ORSTOM, Nouméa, New Caledonia.

Baudry, N. & Calmant, S., 1991. 3-D modelling of seamount topography from satellite altimetry, *Geophys. Res. Lett.*, **18,** 1143–1146.

Baudry, N. & Diament, M., 1987. Shipboard Confirmation of Seasat Predictions in the South Central Pacific, in *Seamounts, Islands and Atolls,* eds Keating, B. *et al.,* Geophys. Monogr. **43,** Am. geophys. Un., Washington, DC.

Baudry, N., Diament, M. & Albouy, Y., 1987. Precise location of unsurveyed seamounts in the Austral archipelago area using SEASAT data, *Geophys. J. R. astr. Soc.,* **89,** 869–888.

Black, M.T. & McAdoo, D., 1988. Spectral analysis of marine geoid heights and ocean depths: constraints on models of lithospheric and sublithospheric processes, *Mar. geophys. Res.,* **10,** 157–180.

Calmant, S., Cazenave, A. & Francheteau, J., 1990. Elastic layer thickening with age of the oceanic lithosphere: a tool for prediction of the age of volcanoes or oceanic crust, *Geophys. J. Int.,* **100,** 59–67.

Cazenave, A., Lago, B., Dominh, K. & Lambeck, K., 1980. On the response of the oceanic lithosphere to sea-mount loads from Geos-3 satellite radar altimeter observations, *Geophys. J. R. astr. Soc.,* **63,** 233–252.

Dixon, T.H., Naraghi, M., McNutt, M.K. & Smith, S.M., 1983. Bathymetric Prediction From SEASAT Altimeter data, *J. geophys. Res.,* **88,** 1563–1571.

Herzfeld, U.C., 1992. Least-squares collocation, geophysical inverse theory and geostatistics: a bird's eye view, *Geophys. J. Int.,* **111,** 237–249.

Goodwillie, A.M. & Watts, A.B., 1993. An altimetric and Bathymetric study of elastic thickness in the Central Pacific Ocean, *Earth planet. Sci. Lett.,* **118,** 311–326.

Journel, A.G., 1989. Fundamentals of geostatistics in Five Lessons, in *Short Courses in geology,* Vol. 8, eds Crawford M.L. & Padovani, E., Am. geophys. Un., Washington, DC.

Jung, W.Y. & Vogt, P.R., 1992. Predicting bathymetry from Geosat ERM and shipborne profiles in the South Atlantic Ocean, *Tectonophysics,* **210,** 235–253.

Kearsely, W., 1977. Non-stationary estimation in gravity prediction problems, *Report* **256,** Dept of Geodetic Sciences, The Ohio State University.

Lambeck, K., 1981a. Flexure of the ocean lithosphere from island uplift, bathymetry and geoid height observations: The Society Islands, *Geophys. J. R. astr. Soc.,* **67,** 91–114.

Lambeck, K., 1981b. Lithospheric response to volcanic loading in the Southern Cook Islands, *Earth planet. Sci. Lett.*, **55**, 482–496.
Lambeck, K. & Coleman, R., 1982. A search for seamounts in the Southern Cook and Austral Region, *Geophys. Res. Lett.*, **9**, 389–392.
Lambeck, K. & Nagiboglu, S.M., 1980. Seamount loading and stress in the Ocean Lithosphere, *J. geophys. Res.*, **85**, 6403–6418.
Larzarewicz, A.R. & Schwank, D.C., 1982. Detection of uncharted seamounts using satellite altimetry, *Geophys. Res. Lett.*, **9**, 385–388.
McNutt, M.N. & Menard, H.W., 1978. Lithospheric Flexure and Uplifted Atolls, *J. geophys. Res.*, **83**, 1206–1212.
Menke, W., 1984. *Geophysical data analysis: Discrete inverse theory*, Academic Press Inc., Orlando, FL.
Moritz, H., 1978. Least square collocation, *Rev. Geophys. Space Sci.*, **16**, 421–430.
Sandwell, D.T., 1984. A detailed view of the South Pacific geoid from satellite altimetry, *J. geophys. Res.*, **89**, 1089–1104.
Sailor, R.V. & LeSchack, A.R., 1987. Preliminary determination of the Geosat radar altimeter noise spectrum, in *J. Hopkins APL Technical Digest*, Vol. 8–2, 182–183, Laurel, MD.
Smith, W.H., 1993. On the Accuracy of Digital Bathymetric Data, *J. geophys. Res.*, **98**, 1959–9603.
Tarantola, A., 1987. *Inverse problem theory, methods for data fitting and model parameter estimation*, Elsevier Science Publisher B. V., Amsterdam, The Netherlands.
Tisseau-Moignard, C., 1979. Modèles de flexure de la lithosphère sous l'effet d'une charge sédimentaire. Application au bassin de Nouvelle Calédonie (Sud-Ouest Pacifique), *Thèse de 3ème cycle* (in French), Université d'Orsay—Paris sud.
Van Wickhouse, R.J., 1973. SYNBAPS (SYNthetic BAthymetric Profiling Systems), *Tech. Rep.*, Naval Oceanographic Office, Washington, DC.
Vogt, P.R. & Jung, W.-Y., 1991. Satellite radar altimetry aids seafloor mapping, *EOS, Trans. Am. geophys. Un.*, **72**, (43), 465 & 468–469.
Watts, A.B., 1979. On Geoid Heights Derived from Geos-3 Altimeter Data Along the Hawaiian-Emperor Seamount Chain, *J. geophys. Res.*, **84**, 3817–3826.
Watts, A.B. & Ribe, N.M., 1984. On Geoid heights and Flexure of the Lithosphere at Seamounts, *J. geophys. Res.*, **89**, 11 152–11 170.

APPENDIX: LINEARIZED FORM OF THE DATA FUNCTIONALS

A1 The surface elements associated with the model parameters

The computation area S is divided in elementary areas $\Delta\Omega(\mathbf{r})$, solution of the integration over $d\theta$ and $d\lambda$ for each area element $[\Delta\theta(\mathbf{r}), \Delta\lambda(\mathbf{r})]$ centred at $[\theta(\mathbf{r}), \lambda(\mathbf{r})]$ with $\theta(\mathbf{r})$ the colatitude and $\lambda(\mathbf{r})$ the longitude:

$$\Delta\Omega(\mathbf{r}) = \int_{\Delta\theta(\mathbf{r})} \sin\theta\, d\theta \int_{\Delta\lambda} d\lambda = \Delta\lambda(\mathbf{r})\left[2\sin\frac{\Delta\theta(\mathbf{r})}{2}\sin\theta(\mathbf{r})\right] \sim \Delta\lambda(\mathbf{r})\Delta\theta(\mathbf{r})\sin\theta(\mathbf{r}). \tag{A1.1}$$

A2 The lithsopheric density contrasts

The elastic deflection of the upper lithosphere under the weight of a volcano generates lateral density contrasts, the gravity signature of which has to be accounted for when dealing with the gravity signature over a marine volcano. Let us consider a standard lithosphere with an upper crustal layer (layer 2) of thickness t_2 and density ρ_2, a lower crustal layer (layer 3) of thickness t_3 and density ρ_3 overlying a mantle of density ρ_m. The volcano density is denoted ρ_v and the water density ρ_w. The sediments filling the flexural moats are assumed to have the density ρ_s. The deflection δw due to a point load P is given by

$$D\,\nabla^4\delta w + \gamma(\rho_m - \rho_s)\delta w = P \tag{A2.2}$$

where D is the stiffness of the equivalent elastic plate and where $\gamma(\rho_m - \rho_s)\delta w$ is the Archimedes force due to the buoyancy of the crust deflected within the lithospheric mantle.

Using $P = \gamma(\rho_v - \rho_w)\Delta\Omega b$ the 3-D solution of eq. (A2.2) is (adapted from Tisseau-Moignard 1979):

$$\delta w = \frac{(\rho_v - \rho_w)R_{sf}^2}{\pi(\rho_m - \rho_s)\alpha^2}\,\mathrm{Kei}\left(\sqrt{2}\frac{\Delta}{\alpha}\right)\Delta\Omega b \tag{A2.3}$$

with

$$\alpha = \sqrt[4]{\frac{4D}{\gamma(\rho_m - \rho_s)}} \tag{A2.4}$$

with Δ the angular distance between the location of the load and that of the computed deflection. Kei is the Kelvin function and α is called the flexural length. In the case of a distributed load $P(\mathbf{r}) = \gamma(\rho_v - \rho_w)\Delta\Omega(\mathbf{r})b(\mathbf{r})$, the deflection $w(\mathbf{r}')$ is given by the sum of the elementary deflections in eq. (A2.3):

$$w(\mathbf{r}') = \frac{(\rho_v - \rho_w)R_{sf}^2}{\pi(\rho_m - \rho_s)\alpha^2}\sum_{\mathbf{r}\in S}\mathrm{Kei}\left(\sqrt{2}\frac{|\mathbf{r}-\mathbf{r}'|}{\alpha}\right)\Delta\Omega(\mathbf{r})b(\mathbf{r}). \tag{A2.5}$$

According to the assumption of an elastic upper lithosphere, this deflection is undergone by all its density interfaces. It then generates three lateral density contrasts at successively the load–layer 2 interface ($\rho_v - \rho_2$), the layer 2–layer 3 interface ($\rho_2 - \rho_3$) and at the Moho ($\rho_3 - \rho_m$).

In the case of a locally compensated structure (*Airy compensation*, $\alpha = 0$), the density of the structure is taken to be identical to that of the root. The thickness $t(\mathbf{r})$ of this root is given by the isostatic equilibrium:

$$t(\mathbf{r}) = b(\mathbf{r})\frac{(\rho_v - \rho_w)}{(\rho_m - \rho_v)}. \tag{A2.6}$$

It is important to note that $w(\mathbf{r})$ and $t(\mathbf{r})$ are linear combinations in $b(\mathbf{r})$. Linear combinations in $w(\mathbf{r})$ or $t(\mathbf{r})$ thus constitute linear combinations in $b(\mathbf{r})$.

A3 Data functionals and linear operators for geoid height data

The geoid height $N(\mathbf{s})$ due to a density anomaly $\Delta\rho$ distributed over a volume V is (Brun's formula):

$$N(\mathbf{s}) = \frac{\Gamma}{\gamma}\Delta\rho\int_V \frac{dv}{\sqrt{a^2 + R^2 - 2aR\cos\psi}}, \tag{A3.1}$$

where ψ is the angular distance between $\mathbf{s}$ and the centre of the mass element dv. Γ is the gravitational constant, γ the mean gravity acceleration at the surface of the Earth, a is the Earth radius and R the distance between the centre of the Earth and the mass element. Using $dv = R^2 \sin\theta\, d\theta\, d\lambda\, dR$, eq. (A3.1) is rewritten:

$$N(\mathbf{s}) = \frac{\Gamma}{\gamma}\Delta\rho\iint_S \sin\theta\, d\theta\, d\lambda \int_{R_{\text{inf}}}^{R_{\text{sup}}} u(R, \psi)\, dR \tag{A3.2}$$

with

$$u(R, \psi) = \frac{R^2}{\sqrt{a^2 + R^2 - 2aR\cos\psi}}. \tag{A3.3}$$

S is the projection of the volume V onto the surface of the Earth. R_{sup} and R_{inf} are the distance from the centre of the Earth to, respectively, the top and the bottom of the mass element. The primitive $\mathcal{U}(R, \psi)$ of $u(R, \psi)$ is:

$$\mathcal{U}(R, \psi \neq 0) = \frac{1}{2}(R + 3a\cos\psi)\sqrt{a^2 + R^2 - 2aR\cos\psi} - \frac{a^2}{2}(1 - 3\cos^2\psi)\,\text{Argsh}\left[\frac{R - a\cos\psi}{a\sin\psi}\right] \tag{A.3.4a}$$

and

$$\mathcal{U}(R, \psi = 0) = -\tfrac{1}{2}R^2 - aR - a^2\,\text{Ln}\,(a - R). \tag{A3.4b}$$

Argsh ( ) is the inverse hyperbolic sine and Ln ( ) the natural Logarithm. ψ is the angular distance between $\mathbf{r}$ and $\mathbf{s}$.

A3.1 Data functionals

The data functional g_{GH} is the discrete form of eq. (A3.2), combined with eq. (A1.1) and calculated for either the bathymetric feature $b(\mathbf{r})$ and the lithospheric density contrasts, the geometry of which is given by $w(\mathbf{r})$ in the context of regional compensation (flexural parameter $\alpha \neq 0$).

In the context of regional compensation, $g_{GH}(\mathbf{s}, \alpha \neq 0)$ is given by:

$$\begin{aligned} g_{GH}(\mathbf{s}, \alpha \neq 0) = \frac{\Gamma}{\gamma}\sum_{\mathbf{r}\in S}\Delta\Omega(\mathbf{r})\{&(\rho_v - \rho_w)[\mathcal{U}(R_{sf} + b(\mathbf{r}), \psi_{sr}) - \mathcal{U}(R_{sf}, \psi_{sr})] + (\rho_s - \rho_2)[\mathcal{U}(R_{sf} + w(\mathbf{r}), \psi_{sr}) - \mathcal{U}(R_{sf}, \psi_{sr})] \\ &+ (\rho_2 - \rho_3)[\mathcal{U}(R_{2/3} + w(\mathbf{r}), \psi_{sr}) - \mathcal{U}(R_{2/3}, \psi_{sr})] + (\rho_3 - \rho_m)[\mathcal{U}(R_m + w(\mathbf{r}), \psi_{sr}) - \mathcal{U}(R_m, \psi_{sr})]\}. \end{aligned} \tag{A3.5}$$

In context of local compensation, $g_{GH}(\mathbf{s}, \alpha = 0)$ is given by:

$$g_{GH}(\mathbf{s}, \alpha = 0) = \frac{\Gamma}{\gamma}\sum_{\mathbf{r}\in S}\Delta\Omega(\mathbf{r})\{(\rho_v - \rho_w)[\mathcal{U}(R_{sf} + b(\mathbf{r}), \psi_{sr}) - \mathcal{U}(R_{sf}, \psi_{sr})] + (\rho_v - \rho_m)[\mathcal{U}(R_m + t(\mathbf{r}), \psi_{sr}) - \mathcal{U}(R_m, \psi_{sr})]\} \tag{A3.6}$$

ψ_{sr} is the angle between $\mathbf{s}$ and $\mathbf{r}$.

A3.2 Linear operators

Eq. (A3.5) and eq. (A3.6) are not linear in the height $h(\mathbf{r})$ of the mass element, whatever it is $b(\mathbf{r})$, $w(\mathbf{r})$ or $t(\mathbf{r})$. A first-order development is then used to generate a linearized functional. Since $h(\mathbf{r}) \ll R$, setting $R_{\text{ref}} = R_{\text{sup}} - \dfrac{h(\mathbf{r})}{2} = R_{\text{inf}} + \dfrac{h(\mathbf{r})}{2}$ (R_{ref} is thus the barycentre of the mass element) in eq. (A3.2), the evaluation of the integral in R, $\mathcal{U}(R_{\text{sup}}) - \mathcal{U}(R_{\text{inf}})$, is replaced by the following first-order development:

$$\mathcal{U}(R_{\text{sup}}) - \mathcal{U}(R_{\text{inf}}) = \left\{\mathcal{U}(R_{\text{ref}}) + \frac{h(\mathbf{r})}{2}\frac{d\mathcal{U}}{dR}\bigg|_{R_{\text{ref}}}\right\} - \left\{\mathcal{U}(R_{\text{ref}}) - \frac{h(\mathbf{r})}{2}\frac{d\mathcal{U}}{dR}\bigg|_{R_{\text{ref}}}\right\} = h(\mathbf{r})u(R, \psi)\big|_{R_{\text{ref}}}. \tag{A3.7}$$

For the sea-floor topography, $h(\mathbf{r})$ represents $b(\mathbf{r})$. For the lithospheric interfaces, $h(\mathbf{r})$ represents $w(\mathbf{r})$ or $t(\mathbf{r})$. The computation

$$N^*(\mathbf{s}) = \frac{\Gamma}{\gamma}\Delta\rho \sum_{\mathbf{r}\in S} \Delta\Omega(\mathbf{r}) \frac{R_{\text{ref}}^2}{\sqrt{a^2 + R_{\text{ref}}^2 - 2aR_{\text{ref}}\cos\psi_{sr}}} h(\mathbf{r}). \tag{A3.8}$$

Now, from eq. (A3.5), eq. (A3.8) and eq. (A2.5), the operator $\mathbf{G}_n(\mathbf{r}, \mathbf{s}, \tau = GH, \alpha \neq 0)$—linearized form relating a model parameter to a datum of geoid height in context of regional compensation—is then, at the nth iteration:

$$\begin{aligned}&\mathbf{G}_n(\mathbf{s}, \mathbf{r}, \tau = GH, \alpha \neq 0)\\ &= \frac{\Gamma}{\gamma}\Delta\Omega(\mathbf{r})\left\{(\rho_v - \rho_w)u\left(R_{sf} + \frac{b_{n-1}(\mathbf{r})}{2}, \psi_{sr}\right) + \frac{(\rho_v - \rho_w)R_{sf}^2}{\pi(\rho_m - \rho_s)\alpha^2}\sum_{\mathbf{r}'}\Delta\Omega(\mathbf{r}')\,\text{Kei}\left(\sqrt{2}\frac{|\mathbf{r} - \mathbf{r}'|}{\alpha}\right)\right.\\ &\left.\times\left[(\rho_s - \rho_2)u\left(R_{sf} + \frac{w_{n-1}(\mathbf{r})}{2}, \psi_{rr'}\right) + (\rho_2 - \rho_3)u\left(R_{2/3} + \frac{w_{n-1}(\mathbf{r})}{2}, \psi_{rr'}\right) + (\rho_2 - \rho_m)u\left(R_m + \frac{w_{n-1}(\mathbf{r})}{2}, \psi_{rr'}\right)\right]\right\}.\end{aligned} \tag{A3.9}$$

From eq. (A3.5), eq. (A3.8) and eq. (A2.6), $\mathbf{G}_n(\mathbf{r}, \mathbf{s}, \tau = GH, \alpha = 0)$—linearized form relating a model parameter to a datum of geoid height in context of local compensation—is, at the nth iteration:

$$\mathbf{G}_n(\mathbf{s}, \mathbf{r}, \tau = GH, \alpha = 0) = \frac{\Gamma}{\gamma}\Delta\Omega(\mathbf{r})(\rho_v - \rho_w)\left[u\left(R_{sf} + \frac{b_{n-1}(\mathbf{r})}{2}, \psi_{sr}\right) - u\left(R_m + \frac{b_{n-1}(\mathbf{r})}{2}, \psi_{sr}\right)\right]. \tag{A3.10}$$

A4 Data functionals and linear operators for gravity-anomaly data

The same developments are made for the gravity anomalies. These are primarily given by:

$$\Delta g(\mathbf{s}) = \Gamma\Delta\rho\int_V \frac{(a - R)\,dv}{\sqrt{a^2 + R^2 - 2aR\cos\psi^3}} \tag{A4.1}$$

and eq. (A4.1) is rewritten as follows:

$$\Delta g(\mathbf{s}) = \Gamma\Delta\rho\iint_S \sin\theta\,d\theta\,d\lambda\int_{R_{\text{inf}}}^{R_{\text{sup}}} v(R, \psi)\,dR \tag{A4.2}$$

with

$$v(R, \psi) = \frac{(a - R)R^2}{\sqrt{a^2 + R^2 - 2aR\cos\psi^3}}. \tag{A4.3}$$

$v(R, \psi)$, the primitive of $v(R, \psi)$ is given by:

$$\begin{aligned}v(R, \psi \neq 0) = &-\sqrt{a^2 + R^2 - 2aR\cos\psi)} + a(1 - 3\cos^2\psi)\,\text{Argsh}\left[\frac{R - a\cos\psi}{a\sin\psi}\right] - a^2\frac{(3 - 4\cos\psi)}{\sqrt{a^2 + R^2 - 2aR\cos\psi}}\\ &- a\frac{(1 - 5\cos\psi + 4\cos^2\psi)(R - a\cos\psi)}{\sin^2\psi\sqrt{a^2 + R^2 - 2aR\cos\psi}}\end{aligned} \tag{A4.4a}$$

and

$$v(R, 0) = \frac{a^2}{a - R} + 2a\,\text{Ln}\,(a - R) - (a - R). \tag{A4.4b}$$

A4.1 Data functionals

Combining eq. (A4.2) and eq. (A1.1) the data functional in case of regional compensation $g_{GA}(\mathbf{s}, \alpha \neq 0)$ is given by:

$$\begin{aligned}g_{GA}(\mathbf{s}, \alpha \neq 0) = \Gamma\sum_{\mathbf{r}\in S}\Delta\Omega(\mathbf{r})\{&(\rho_v - \rho_w)[\mathcal{V}(R_{sf} + b(\mathbf{r}), \psi_{sr}) - \mathcal{V}(R_{sf}, \psi_{sr})] + (\rho_s - \rho_2)[\mathcal{V}(R_{sf} + w(\mathbf{r}), \psi_{sr}) - \mathcal{V}(R_{sf}, \psi_{sr})]\\ &+ (\rho_2 - \rho_3)[\mathcal{V}(R_{2/3} + w(\mathbf{r}), \psi_{sr}) - \mathcal{V}(R_{2/3}, \psi_{sr})] + (\rho_2 - \rho_m)[\mathcal{V}(R_m + w(\mathbf{r}), \psi_{sr}) - \mathcal{V}(R_m, \psi_{sr})]\}.\end{aligned} \tag{A4.5}$$

In case of local compensation, $g_{GA}(\mathbf{s}, \alpha = 0)$ is given by:

$$g_{GA}(\mathbf{s}, \alpha = 0) = \Gamma\sum_{\mathbf{r}\in S}\Delta\Omega(\mathbf{r})\{(\rho_v - \rho_w)[\mathcal{V}(R_{sf} + b(\mathbf{r}), \psi_{sr}) - \mathcal{V}(R_{sf}, \psi_{sr})] + (\rho_v - \rho_m)[\mathcal{V}(R_m + t(\mathbf{r}), \psi_{sr}) - \mathcal{V}(R_m, \psi_{sr})]\}. \tag{A4.6}$$

A4.2 Linear operators

The linearized form $\Delta g^*(\mathbf{s})$ of eq. (A4.1) is:

$$\Delta g^*(\mathbf{s}) = \Gamma \Delta\rho \sum_{\mathbf{r}\in S} \Delta\Omega(\mathbf{r}) \frac{(a - R_{\text{ref}})R_{\text{ref}}^2}{\sqrt{a^2 + R_{\text{ref}}^2 - 2aR_{\text{ref}}\cos\psi_{sr}}^3} h(\mathbf{r}). \tag{A4.7}$$

From eq. (A4.5), eq. (A4.7) and eq. (A2.5), the operator $G_n(\mathbf{r}, \mathbf{s}, \tau = GA, \alpha \neq 0)$—linearized form relating a model parameter to a datum of gravity anomaly in context of regional compensation—is then, at the nth iteration:

$$\begin{aligned}
&\mathbf{G}_n(\mathbf{s}, \mathbf{r}, \tau = GA, \alpha \neq 0) \\
&= \Gamma\Delta\Omega(\mathbf{r})\left\{(\rho_v - \rho_w)v\left(R_{sf} + \frac{b_{n-1}(\mathbf{r})}{2}, \psi_{sr}\right) + \frac{(\rho_v - \rho_w)R_{sf}^2}{\pi(\rho_m - \rho_s)\alpha^2} \sum_{\mathbf{r}'\in S} \Delta\Omega(\mathbf{r}')\,\text{Kei}\left(\sqrt{2}\frac{|\mathbf{r} - \mathbf{r}'|}{\alpha}\right)\right. \\
&\left. + \left\{(\rho_v - \rho_2)v\left(R_{sf} + \frac{w_{n-1}(\mathbf{r})}{2}, \psi_{rr'}\right) + (\rho_2 - \rho_3)v\left(R_{2/3} + \frac{w_{n-1}(\mathbf{r})}{2}, \psi_{rr'}\right) + (\rho_3 - \rho_m)v\left(R_m + \frac{w_{n-1}(\mathbf{r})}{2}, \psi_{rr'}\right)\right\}.
\end{aligned} \tag{A4.8}$$

From eq. (A4.5), eq. (A4.7) and eq. (A2.6), the operator $\mathbf{G}_n(\mathbf{r}, \mathbf{s}, \tau = GA, \alpha = 0)$, linearized form relating a model parameter to a datum of gravity anomaly in context of local compensation, is:

$$\mathbf{G}_n(\mathbf{s}, \mathbf{r}, \tau = GA, \alpha = 0) = \Gamma\Delta\Omega(\mathbf{r})(\rho_v - \rho_w)\left[v\left(R_{sf} + \frac{b_{n-1}(\mathbf{r})}{2}, \psi_{sr}\right) - v\left(R_m + \frac{t_{n-1}(\mathbf{r})}{2}, \psi_{sr}\right)\right]. \tag{A4.9}$$

A5 *A priori* information

If the structure that the submarine topography of which is to be computed is known to be elongated, this can be entered amongst the *a priori* information. Indeed, the auto-covariance of the topography also reflects this anisotropy. It can thus be modelled by a correlation length that varies with the azimuth in the computation of the *a priori* covariance matrix. In an elliptic approximation, three values of correlation lengths are necessary for three azimuths (adapted from Kearsley 1977):

$$L_c(\alpha) = \left[L_c(0)\cos\alpha - L_c\left(\frac{\pi}{2}\right)\sin\alpha\right](\cos\alpha - \sin\alpha) + L_c\left(\frac{\pi}{4}\right)\sin 2\alpha \tag{A5.1}$$

where α is the azimuth of the rr' arc.